Effect of Temperature on Microparticle Rebound Characteristics at Constant Impact Velocity

Matthew Keith Murdock

Thesis submitted to the faculty of the Virginia Polytechnic Institute and State University
in partial fulfillment of the requirements for the degree of

Master of Science
In
Mechanical Engineering

Wing F. Ng (Committee Co-Chair)
Srinath V. Ekkad (Committee Co-Chair)
Danesh K. Tafti

December 10, 2013
Blacksburg, VA

Keywords: Sand Ingestion, Coefficient of Restitution, Particle Impact

Effect of Temperature on Microparticle Rebound Characteristics at Constant Impact Velocity

Matthew Keith Murdock

Abstract

Many gas turbine engines operate in harsh environments where the engine can ingest solid particles. Particles can accelerate the deterioration of an engine and reduce the engine's service life. Understanding particle interactions with the materials used in gas turbines, at representative engine conditions, can improve the design and development of turbomachinery operating in particle laden environments. Coefficient of Restitution (COR) is a measure of the particle/wall interactions and is used to study erosion and deposition. This study presents data taken using the Virginia Tech Aerothermal Rig. Arizona Road Dust (ARD) of 20-40 μm is injected into a flow field to measure the effects of temperature and velocity on particle rebound from a polished high temperature material coupon. The high temperature coupon was tested at different temperatures of ambient (300K), 873K, 1073K, 1173 K, 1223 K, 1273 K, and 1323 K while the velocity of the flow field was held constant at 28 m/s or 70 m/s. The impingement angle of the coupon was varied from 30° to 80° for each temperature tested. The results show an increase in deposition as the temperature approaches the melting temperature of sand. The results have also been compared to previously published literature.

Acknowledgements

I first would like to thank my family - my Mom Susan, Dad Joe, and Brother Ryan for all of their love and support over the years. Thank you for always encouraging me. To Chelsea, thank you for always listening to me and putting things into perspective. I would not be here without your love and support.

A special thank you goes to Jacob Delimont for teaching me everything about this project and all the long hours we spent researching. I want to thank Dr. Ng and Dr. Ekkad for guiding the project, pushing us to meet our goals, and their insight and support. Raul Otero, David Mayo, and Avi Friedman deserve recognition for helping run our experiments, odd jobs, and the favorite task of polishing coupons. To Sukhjinder Singh and Dr. Tafti, thank you for all the thoughtful discussions and insight on the project. Thank you Diana Israel for placing all of our orders and everything else you do to keep this project running.

This work would not have been completed without the guidance of Brett Barker, Kwen Hsu, Paul Davis, and M.S. Anand.

Table of Contents

List of Figures

List of Tables

Nomenclature

a	Acceleration
ARD	Arizona Road Dust
C_d	Drag Coefficient
CFD	Computational Fluid Dynamics
COR	Coefficient of Restitution
d	Diameter
e	Coefficient of Restitution (COR)
F_d	Drag Force
L	Length
m	Mass
PDF	Probability Density Function
PTV	Particle Tracking Velocimetry
Re	Reynolds Number
Stk	Stokes Number
t	Time
V	Velocity
$\bar{x}$	Mean

Greek

β	Impact angle
ρ	Density
μ	Viscosity

subscript

N	Normal
p	Particle
T	Tangential
∞	Freestream

1. Introduction

1.1 Background

Air and land based gas turbines are a popular source of mechanical power. Many of these engines are operated in particle laden environments that are detrimental to engine performance. Aircrafts operating in remote locations or at low altitude can be subjected in to particle ingestion. Figure 1 displays a picture of an aircraft operating in a desert environment. Engines operating in desert environments will be subject to sand, dust, and other particulate. Natural disasters such as volcanic eruptions and dust storms can send particulate to aircraft cruising altitudes. Particle ingestion can reduce engine life and performance through erosion and deposition.

Figure 1. V-22 Osprey [Department of Defense]

Sand and dust affect gas turbine engines in several ways. In the cold section of the engine, erosion is the primary mechanism of damage. Once the particulate passes through the burner, sand melting and deposition becomes the primary mechanism of sand particulate damage. Deposition on gas turbine blades and vanes causes changes in aerodynamic profiles, deposits of surface coatings on combustor and turbine components, deterioration of film cooling efficiency, and blockages of cooling systems, all of which can lead to premature engine failure.

In the past, erosion and deposition has been modeled in several computational studies for gas turbines. These studies have used empirical impact correlations and analytical models to determine the behavior of the particles at impact. The current study expands the data available for empirical impact correlations by presenting impact and rebound characteristics of microparticle sand at temperatures near the melting point of sand. This will enable more accurate models and computational analysis of sand transport in gas turbines.

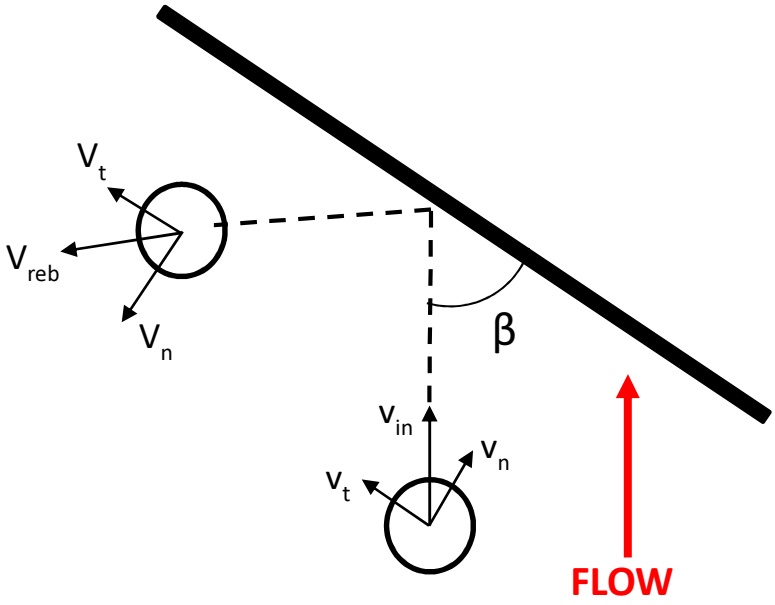

Figure 2. Diagram of a particle impacting a plate

Figure 2 displays a diagram of a particle impacting a plate. The definition of an impact is one object striking against another. There are two types of impact: elastic and inelastic. In an elastic impact there is no loss of kinetic energy. For an inelastic impact, some of the kinetic energy is lost. Particle deformation, friction, and adhesion are different forces that will cause energy transfer in an impact. The loss in kinetic energy during a collision can be quantified using the coefficient of restitution (COR). Coefficient of restitution is a measure of the particle/wall interactions and is used to study erosion and deposition. COR is defined as:

1) $$e = \frac{v_{reb}}{v_{in}}$$

where v_{reb} is the velocity after impact and v_{in} is the incoming velocity before impact. A perfectly elastic impact will have a COR equal to 1. A perfectly inelastic impact will have a COR of 0 and the colliding objects will stick together. Figure 3 displays a diagram of a particles trajectory before and after impact. The solid lines in Figure 3 represent the particles actual velocity while the dotted lines represent the normal and tangential components of velocity.

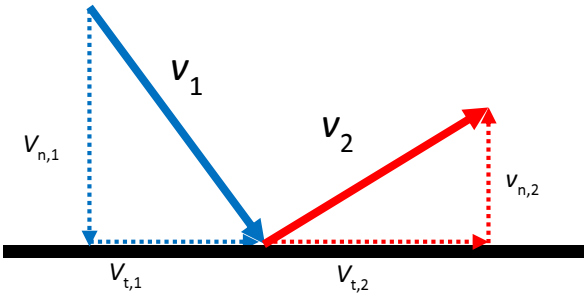

Figure 3. Diagram of incoming and rebounding particle trajectories

COR for the normal and tangential components of velocity are also important quantities for studying particle impacts. The normal and tangential CORs are defined as:

2) $$e_N = \frac{v_{N,2}}{v_{N,1}}$$

3) $$e_T = \frac{v_{T,2}}{v_{T,1}}$$

where $v_{N,2}$ is the normal component of the rebounding velocity, $v_{N,1}$ is the normal component of the incoming velocity, $v_{T,2}$ is the tangential component of the rebounding velocity, and $v_{T,1}$ is the tangential component of the incoming velocity. COR depends on many factors such as particle velocity, particle size, temperature, surface roughness,

surface hardness, particle spin, particle shape, and material properties.

1.2 Past Studies

Some of the first studies of impact mechanics were done by Goldsmith [1] in the 20th century. From this work COR is found to decrease with increasing velocity, increasing particle size, and decreasing surface hardness. Tabakoff [2] confirms that in general COR decreases as particle velocity increases. Li *et. al.* [3] studied 70 μm mean diameter SS316 spheres impacting a silicon crystal wafer at different angles and velocities. The velocities measured were very low, 1.6 m/s, 1.05 m/s, and .45 m/s. The COR was relatively constant at 0.7 for angles between 50° and 85°. Microparticle adhesion is an issue at these low velocities and contributes to the low COR values.

There are a few studies that investigate the effect of surface roughness on COR. Sommerfeld and Huber [4] studied the impacts of 100 and 500 μm glass beads and 100 μm non-spherical quartz particles on different materials. From the study they found that rougher surfaces and more oblong particles tend to have a lower COR and wider scatter due to local deformation. This study also documents a phenomena called the shadow effect. At shallow angles of impact, there is a large rise in the normal COR. This is due to surface and particle irregularities compounding with already small magnitudes of normal velocity. This effect is magnified with smaller particles but reduces as angle of impact increases. Whitaker *et. al.* [20] studied the effects of surface roughness on COR for 150-1,000 μm quartz particles at impact angles from 0°-90° using a particle shadow velocimetry technique. The surface roughness of the aluminum target was varied from 0.8-8.0 μm. From this study it was found that COR decreases slightly with increasing surface roughness.

Past studies have mostly neglected the effects of temperature on COR. Only a few studies are relative to the current research. Mok and Duffy [5] studied solid steel balls impacting cylindrical targets made from 6061-T6 aluminum. The balls impacted the target at 90° with a range of velocities from 0-5 m/s and temperatures from 294-755 K. Temperature did have an effect on the COR for the steel ball/aluminum impact. It

was found that as temperature increased, COR decreased. Brenner *et. al.* [6] studied the impacts of three types of iron spheres on aluminum oxide covered iron plates at 973 and 1073 K at 90° impact angle. COR results were presented for velocities up to 3 m/s. COR was found to decrease as the temperature increased.

Tabakoff *et. al.* [7-10] completed a number of studies on the erosive effects of particles on metals. COR has been used in these studies to find a correlation between COR and erosion. These works show that erosion is mainly a function of the tangential COR. These works also clearly show that COR is a statistical function. Wakeman and Tabakoff [9] studied the erosive behavior of 150-180μm quartz sand at temperatures up to 978 K and velocities up to 274 m/s at different impact angles. It was concluded that as velocity increased for the erosive data, a power law relationship fit the data very well. The coefficients for the relationship vary with material and angle of impact. Tabakoff *et. al.* [8] studied 150 μm sand particles impacting several turbomachinery target materials at 90.85 m/s for different angles of impact. The COR trends for all of the materials were similar, but the characteristics of the COR were different for each of the materials. Reagle and Delimont [11, 12] tested the effects of temperature and velocity on COR for sand particles. In those studies, velocity was not controlled independently of temperature and the velocity increased with temperature. The current study controls velocity independent of temperature allowing for the effects of temperature to be studied.

Several studies have been performed to study the effect of temperature on particle deposition. Walsh *et. al*. [13] performed sand deposition studies and found that the temperature at which sand begins to deposit to be between 1273 K and 1353 K in their experimental setup. Crosby and Bons [14] found that fly ash experiences a sharp decrease in deposit quantities at temperatures below 1233 K. All of these as well as several others have studied deposition patterns, but have not characterized impact characteristics. These studies do indicate that deposition should be seen in the VT Aerothermal Rig at 1273 K and 1323 K.

COR has not been documented at near-deposition temperatures for engine representative sand microparticles at different angles. More study is needed before particle transport and energy transfer mechanisms of microparticles can be confidently included in computation models. This study provides new insight as to the effect of

temperature and velocity on particles that will help bridge the gap. The companion works to this study [15, 19] investigate the effects of temperature on COR for different target materials 304 stainless steel and a nickel alloy Hastelloy X. The results are immediately applicable to enhancing the accuracy of numerical simulations.

1.3 Objectives and Scope

The objective of this study is to determine the effects of temperature on the COR of microparticle sand at a constant impact velocity. A test coupon made of a high temperature alloy was tested at different angles of impact ranging from 30° to 80°. The tests will be performed at a constant velocity of 28 m/s or 70 m/s. From previous studies [5-6] it was found that COR decreases as temperature increases. The efforts of this study hope to verify this result at gas turbine relative conditions.

This study also investigates how deposition affects COR. From previous research [13] the melting temperature of sand is about 1323 K, the highest temperature tested in this study. At this temperature significant depostition is predicted to occur on the coupon face. It is expected that with the increase in deposition a sharp decrease in the COR will occur.

This study is being completed in conjunction with a CFD modeling effort. The work done in the current study is being used to validate the CFD to better predict the behavior of the particles. This work will be incorporated into computational models to help improve the design of turbomachinery components susceptible to particle ingestion.

2 Experimental Method

2.1 Aerothermal Rig

The Virginia Tech Aerothermal Rig was donated by Rolls Royce to Virginia Tech in 2010. It was previously used in Indianapolis, Indiana, for heat transfer studies by Nealy *et. al.* [16] and Hylton *et. al*. [17]. The original operation specifications for this rig were reported by Rolls Royce as 2.2 kg/s at a maximum pressure of 16 atm and temperature of 2033 K. The VT Aerothermal Rig was used in conducting all of the experiments discussed in this paper

The rig has been modified from its original configuration to allow sand to be injected immediately downstream of the burner. Figure 4 is an image of a CAD model of the VT Aerothermal Rig showing its layout in the current configuration. The rig was used previously by Reagle [11, 12] to study sand ingestion at temperatures lower than 1073 K. Since the work by Reagle, the equilibration tube has been changed to allow for a higher maximum operating temperature. The current maximum test section temperature of the rig is 1323 K.

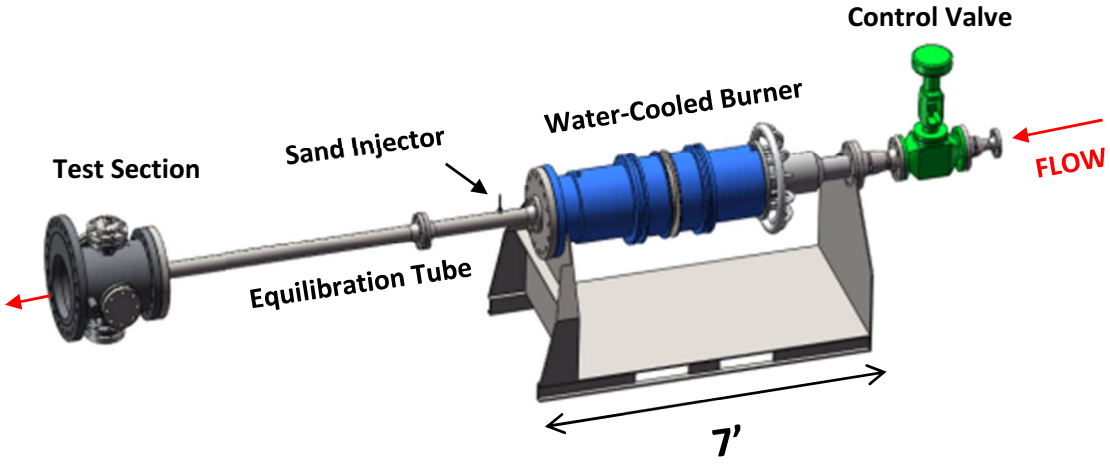

Figure 4. VT Aerothermal Rig

A compressor supplies compressed air to a buffer tank at a mass flow rate of 0.15 kg/s. A series of regulator valves control the flow rate of the air before it goes through the main control valve, which is used to make fine adjustments. The regulator control valves are adjustable so that any mass flow rate less than 0.15kg/s can be maintained. These regulators allow the mass flow rate of the rig to be controlled precisely, which in turn allows temperature and velocity to be controlled independently. Figure 5 displays a picture of the regulator valves used in the VT Aerothermal Rig. The air flow passes from the buffer tank to the regulators, then to the main control valve.

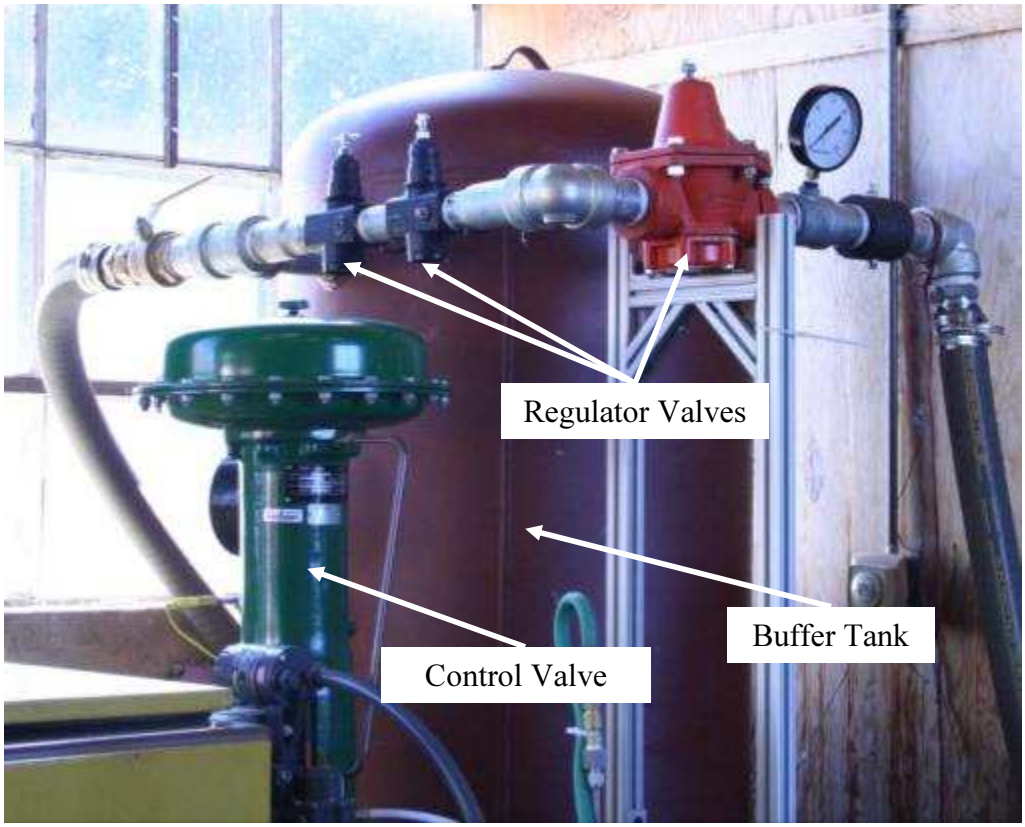

Figure 5. Picture of the Regulator Valves

After passing through the control valve, the air flow passes through the sudden-expansion, water-cooled burner that heats the flow using methane as fuel. The sand particles are entrained in a flow separate from the main flow and are injected into the main flow after the burner. The flow travels through the 7.62 cm diameter, 1.82 m equilibration tube to allow the sand particles to reach the temperature and velocity of the

flow. The flow then exits the equilibration tube as a free jet in the test section and impinges on the test coupon. During each test, a sufficient amount of time is allowed for the temperature of the rig to reach equilibrium before sand particles are injected and measurements of the particles are taken.

A CAD image of the test section without the outer casing walls is shown in Figure 6. The figure shows the test coupon support that can be rotated in 10° increments. This allows for various angles of impingement to be studied. A quartz viewing window in the top flange allows for a camera to view the test coupon. The test section also has a quartz laser access port to allow illumination of the coupon and particles during testing. The test coupon on which the impacts occur is 3.81 cm by 6.35 cm. The coupon is rectangular in shape to allow for a sufficient area to be projected normal to the flow when testing at shallow impingement angles. The test coupon is made from a high temperature material. The coupon is polished to a mirror finish with a measured RMS roughness less than 0.2μm before every testing run to ensure surface roughness effects a minimalized.

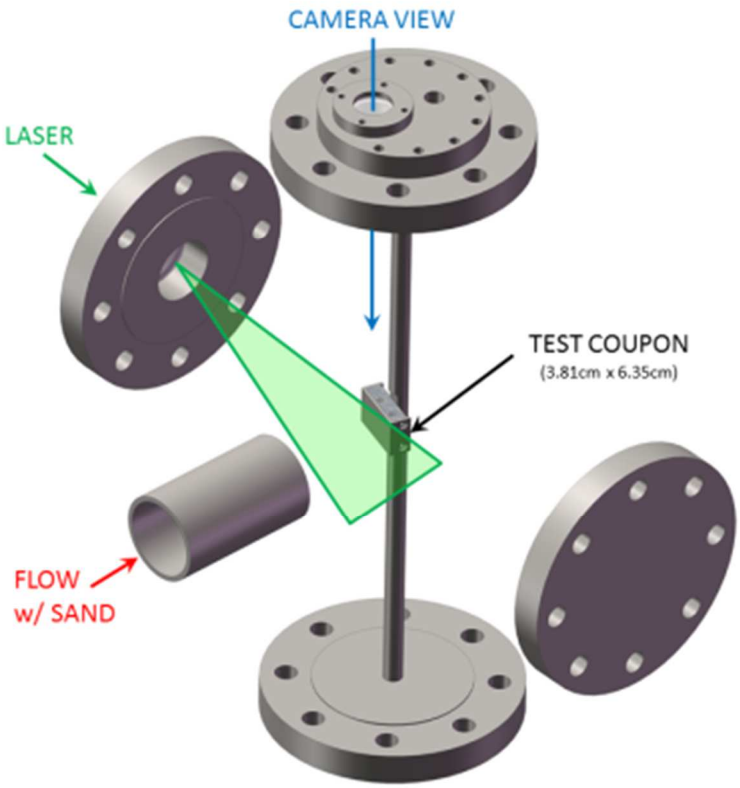

Figure 6. Schematic of instrumentation setup

2.2 Instrumentation

In order to determine the velocity of the flow exiting the equilibration tube, a Pitot-static probe is mounted to a traversing mechanism and placed at the exit of the equilibration tube. Because the probe is mounted to a traverse mechanism it can be placed in the flow to verify test conditions prior to the run and then removed so as not to be damaged or clogged by sand while particles are being injected into the flow. The Pitot-static probe survey, seen in Figure 7, was taken at a distance of 8.13cm upstream from the coupon face to quantify the fully developed velocity profile. The probe is moved out of the test section during particle injection.

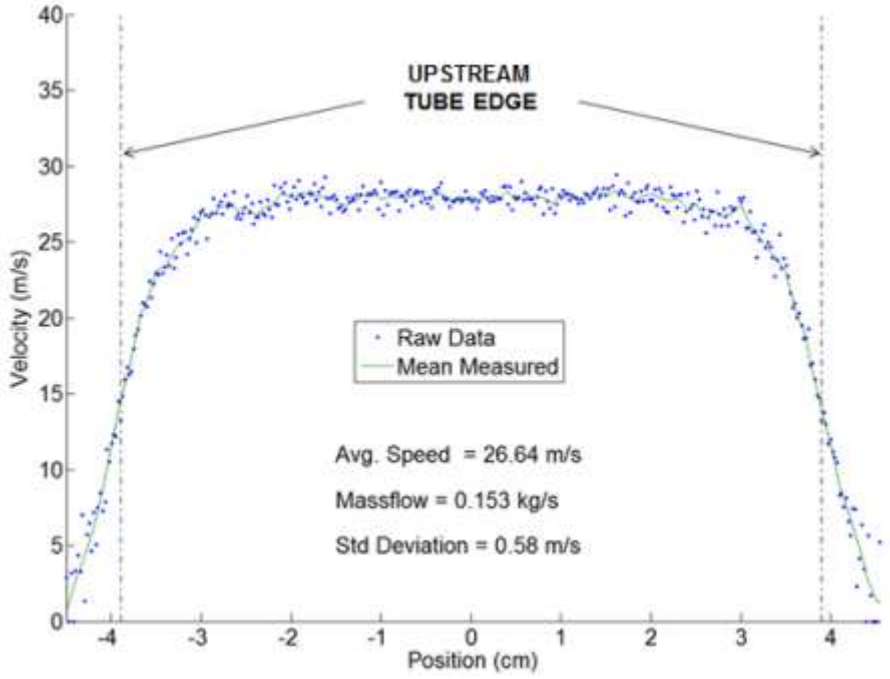

Figure 7. Pitot-Static Traverse 8.13cm Upstream of Coupon at Ambient

To measure the temperature of the air exiting the equilibration tube, a type K thermocouple is placed above the coupon. Additionally, a thermocouple is buried inside the metal of the coupon itself, and sealed with high temperature cement, in order to accurately measure the temperature of the coupon. There are many other thermocouples which are also placed on and in the rig. These thermocouples are used to insure that the

rig has reached equilibrium temperature and to make sure that the rig does not go over its safe temperature limits.

A Litron Nd:YAG laser is used to illuminate the particles in the test section. The laser can be set to emit up to 135mJ per laser pulse at 532 nm wavelength. For the camera settings used in this experiment, it was found that setting the laser to 55mJ produced the best images. The thickness of the laser sheet where it intersects the coupon is ~4mm. The camera used is a Dantec Dynamics® FlowSense camera equipped with a Zeiss® Makro-Planar 2/50 lens. Figure 6 shows the relation of the laser light, camera, equilibration tube, and coupon. The camera is a monochrome camera which captures images with a 2048x2048 resolution. The laser-camera system is able to refresh at a rate of 7.4 Hz between image pairs captured. The camera is focused such that a single particle is captured in one or two pixels on each image. With the air velocity set to 28 m/s, it was found that 15 μs between images was the best setting for the laser and camera image pair speed. When the air velocity was set to 70 m/s, it was found that 6 μs between images was the best setting for the laser and camera image pair speed. These times allow the particles to move up to ~9 pixels between images. This particle movement is enough distance to get an accurate measure of the particle's velocity. If the particles move too far between the two images it becomes very difficult to correctly match a particle from the first image with a particle from the second image. This produces many false velocity vectors. The time between images is small enough to almost eliminate the possibility of false velocity vectors.

2.3 Particles

The sand particles used for this test are Arizona Road Dust (ARD). The particle size of the ARD used for this test was a narrow size range of 20-40μm. The mean size is 29.25μm by volume for this size range. The numerical mean particle size was calculated from particle batch analysis provided by the particle manufacturer of the ARD used in the experiments. A narrow size range of particles is extremely important so that the possible effects of particle size do not contaminate the test results. The chemical composition as

well as description of particle size distribution of this test dust range is reported in Table 1. and Table 2 as given by the manufacturer. The chemical composition reported is the bulk chemical composition of the ARD. Individual particles will vary in composition.

Table 1. Test Dust Chemical Composition

Chemical	% Weight	Melting Point (K)
Quartz (SiO2)	68-76	1983
Aluminum Oxide (Al2O3)	10-15	2323
Iron Oxide (Fe2O3)	2-5	1838
Calcium Oxide (CaO)	2-5	2845
Potassium Oxide (K2O)	2-5	373 (boiling)
Sodium Oxide (Na2O)	2-4	1548
Magnesium Oxide (MgO)	1-2	3073
Titanium Dioxide (TiO2)	0.5-1	3116

Table 2. 20-40μm ARD Size Properties

Particle Size (μm)	Cumulative Percent Volume (%)
< 15.10	< 1.16
< 29.25	< 50
< 40.91	< 99.04

Small microparticles have a tendency to clump together while being stored due to moisture. In order to achieve accurate test results for microparticles, the particles cannot be allowed to clump together. To avoid clumping, it is necessary to heat the particles for

several hours in an oven to remove all moisture from the particles. This prevents much of the clumping that would otherwise occur.

2.4 Test Conditions

In previous works published using this experimental setup by Reagle and Delimont [11, 12] there was no method for precisely controlling the mass flow rate in the test rig. This meant that as the air temperature was raised the velocity of the flow increased as well. As discussed in the section on the VT Aerothermal Rig, modifications made for this study allow a constant velocity at multiple temperatures. The velocities chosen for this work were 28 m/s and 70 m/s. Also it is important to note that the temperature of the metal coupon is substantially lower than the air and particle temperature. This lower temperature is due to conduction through the support and radiation heat transfer losses that affect the coupon. Table 3 below shows the test conditions for the experiments described in this paper. These test conditions were chosen after studying the experiments of Walsh *et. al.* [13] and Crosby and Bons [14]. Temperatures near and below the critical temperature were chosen to observe the effects of near melting temperature on COR. An additional run was performed at 1073 K to verify the repeatability of the data. It was found that the data was repeatable within 0.01 on the COR scale.

Table 3. Test Temperatures and Velocities

Air Temp (K)	Coupon Temp. (K)	Bulk Velocity (m/s)
~300	~300	28
873	803	28
1073	933	28
1073	933	70
1173	1033	70
1273	1133	70
1323	1183	70

3 Data Reduction Method

3.1 Method

The data reduction method used for this experiment is very similar to that which was used in past studies [11, 12] involving this experimental setup. A few significant changes have been made to the method to improve accuracy. Because the particle velocity is always measured at a distance from the target coupon, some velocity correction is needed. Past works by other researchers using similar methods of determining particle velocity have assumed that the measured velocity at some distance from the target was the velocity with which the particle would arrive at or leave the target. While this may be a valid assumption for large particles, it is not true for smaller particles which are strongly influenced by the fluid flow. This necessitates the use of a velocity correction in order to obtain the velocity at the moment of impact with the target coupon.

3.2 Particle Tracking

The Particle Tracking Velocimetry (PTV) method involves implementing a band pass filter on the raw image to remove large objects (coupon, thermocouples, etc.), locating the particles, and then using a radius of gyration calculation to find the particle centroid to sub-pixel accuracy. After the particle locations have been determined, the particles are then correlated between the image pair to determine particle velocity. If there is more than one possible correlation option within the circle of possible movement for the particle, then that particle velocity track is disregarded. Figure 8 displays tracked particles with their velocity vectors. The blue circles correspond to the particles' position in the first image and the red circles correspond to the particles' position in the second image of the image pair. At 28 m/s the image pair is taken 15 μs between images.

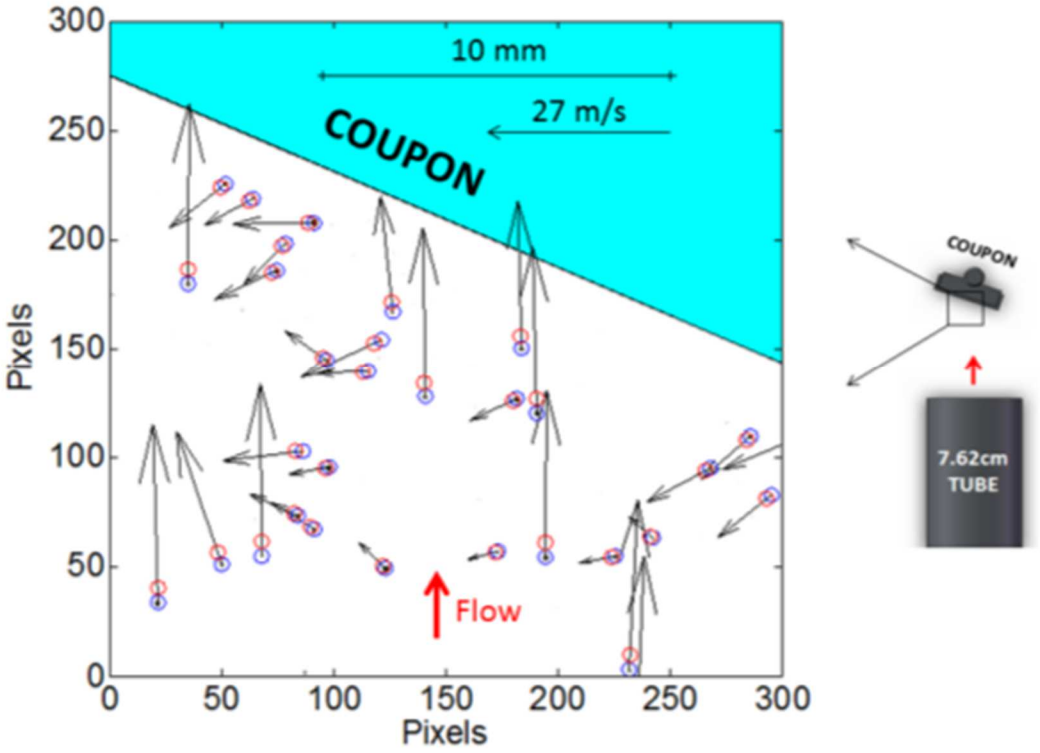

Figure 8. Results from Particle Tracking Code

Once the particles' position between images is determined, the velocity is calculated. A simplified analysis assumes that the drag force is the only force influencing the particle. The effects of particle spin have been neglected and the particle is assumed to be a smooth sphere. First, the forces on the particle are defined using Newton's second law:

4) $$\boldsymbol{F_d = ma \quad \rightarrow \quad a = F_d/m}$$

where m is the mass of the particle, a is acceleration, and the drag force, F_d, is defined as

5) $$\boldsymbol{F_d = \frac{1}{8}\pi C_d d_p^2 \rho_g v_{rel}^2}$$

where d_p is the diameter of the particle, ρ_g is the density of the flow, v_{rel} is the difference between the particle velocity and flow velocity, and C_d is the drag coefficient. The drag

coefficient is calculated using a correlation developed by Morrison [21] using Reynolds numbers up to 10^6 for smooth spheres.

6) $$C_d = \frac{24}{Re} + \frac{2.6\left(\frac{Re}{5.0}\right)}{1+\left(\frac{Re}{5.0}\right)^{1.52}} + \frac{0.411\left(\frac{Re}{263{,}000}\right)^{-7.94}}{1+\left(\frac{Re}{263{,}000}\right)^{-8.00}} + \frac{Re^{0.80}}{461{,}000}$$

The velocity can be calculated using:

7) $$v(t) = v_0 + at$$

where v_o is the velocity at t=0. Equation 4 can be substituted into Equation 7 to solve for the velocity of the particle. The total velocity of the particle is found and is later broken into x and y components. The relative velocity of the particles at the exit of the pipe is very close to zero. As the particles approach the coupon face, the flow field begins to change and shifts the particles trajectory. The particles used in this experiment have very low Stokes numbers and are highly influenced by the flow field.

The Stokes number (Stk) is the ratio of particle relaxation time to fluid relaxation time or characteristic dimension of an obstruction. The Stk quantifies the degree to which particles suspended in a fluid flow will follow the fluid motion. This means that a particle with a Stk much larger than one will not follow the fluid flow, but instead its momentum will force it to keep traveling in its original direction. The equation used to calculate the Stk is shown in the following equation,

8) $$Stk = \frac{\rho_p d_p^2}{18\mu}\frac{V_\infty}{L_c}$$

where ρ_p is density of the particle, d_p is diameter of the particle, V_∞ is fluid velocity, μ is fluid viscosity, and L_c is the characteristic length of the system. For this experiment, L_c is defined as the length of the coupon. The Stk determines how the particle will behave in a fluid flow. Particle impact characteristics are not directly affected by the particle Stk; however, it is still important to know the Stk of the particles, because at very low Stk no particle impact on the target coupon will occur. Figure 9 displays the tracked particle

history of incoming and rebounding particles. From the figure, particles that are closer to the edge of the coupon are influenced by the flow field and have a curved incoming trajectory. The Stk at the different experimental conditions is given in Table 4 below.

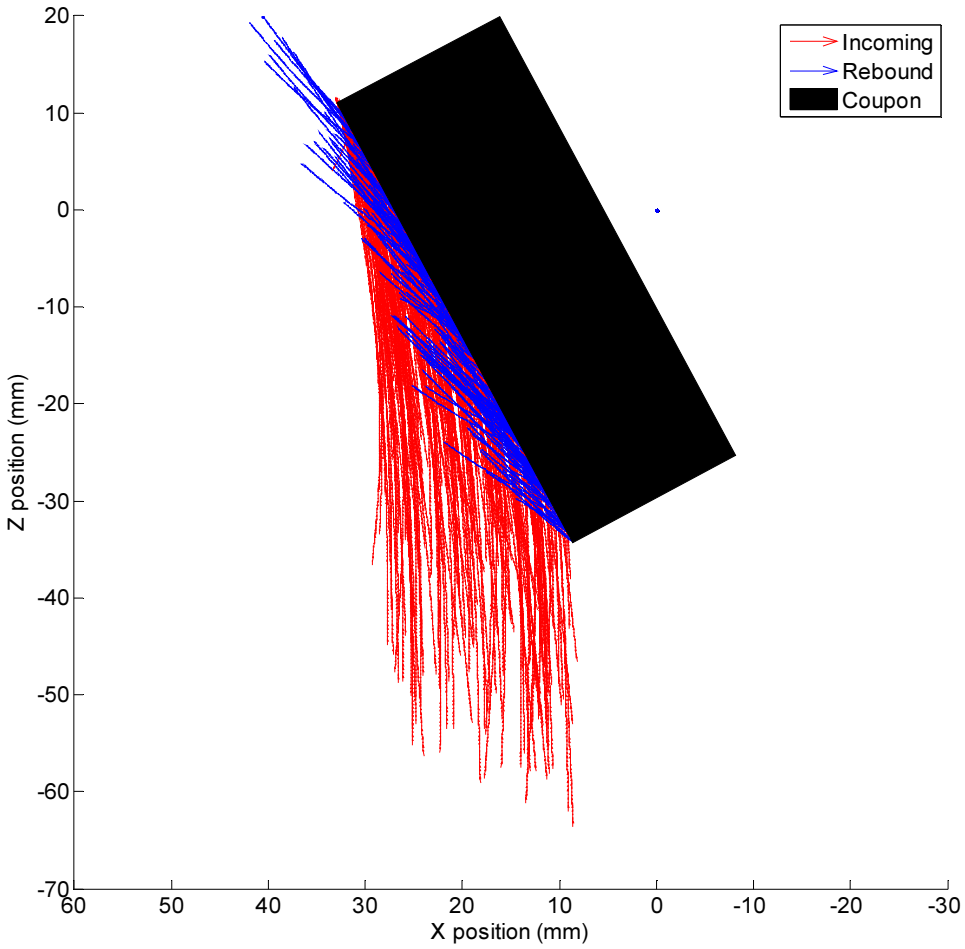

Figure 9. Particle trace history

Table 4. Test Dust Stk Values

Test Condition (K)	Bulk Velocity (m/s)	Stk 20μm Sand	Stk 40μm Sand
300	28	1.15	4.58
873	28	0.55	2.18
1073	28	0.48	1.92
1073	70	1.20	4.81
1173	70	1.14	4.56
1273	70	1.09	4.35
1323	70	1.06	4.25

Once the particle velocity has been measured, the velocity is used as an initial condition for a Lagrangian particle tracking algorithm which uses a flow field calculated from ANSYS CFX for the Eulerian phase of the calculation. This computational flow field is validated against velocity surveys taken with the Pitot-static probe immediately upstream of the coupon to ensure accuracy. Although the basic method used by Reagle and Delimont [11, 12] in previous works has been retained, one significant change has been made to the particle tracking algorithm. In the method used for this work, there is a limit to how far a rebounding particle may be from the coupon to still be used in the data reduction scheme. This limit is set to 50 time steps of the Langrangian particle path algorithm. This means that rebounding particles must have travelled less than 2cm from the point of impact to be counted. This constraint helps to eliminate any error that could be created by use of the Langrangian correction to the particle velocity.

3.3 Coefficient of Restitution Calculation

In order to determine the COR, incoming and rebounding particles are sorted into bins by the location of impact on the target coupon. The width of the coupon area that is allocated to each bin is 1mm. A mean velocity of incoming particles as well as a mean of

the rebounding particles at each location is then calculated. Calculating the probability distribution of the COR around the mean is a complicated task.

In order to properly calculate the distribution of the COR about the mean, it is necessary to perform a ratio distribution of V_2 and V_1. The equation for the ratio distribution of two variables was derived by Hinkley in his 1969 work [18]. This derivation requires that the two distributions be Gaussian, which is verified during the data reduction process. Because V_2 and V_1 are independent over the 1mm width of coupon face, the equation for the probability density function (pdf) of the ratio distribution can be simplified to the following format:

9)

$$\boldsymbol{p.d.f.(z)} = \frac{\boldsymbol{b(z)} * \boldsymbol{c(z)}}{\sqrt{(2\pi)}\boldsymbol{\sigma_1\sigma_2 a^3(z)}} \left[\boldsymbol{\Phi}\left(\frac{\boldsymbol{b(z)}}{\boldsymbol{a(z)}}\right) - \boldsymbol{\Phi}\left(-\frac{\boldsymbol{b(z)}}{\boldsymbol{a(z)}}\right)\right] + \frac{\mathbf{1}}{\boldsymbol{a^2(z)\pi\sigma_1\sigma_2}} \boldsymbol{e}^{-\frac{1}{2}\left(\frac{\bar{x}_1^{\,2}}{\sigma_1^2} + \frac{\bar{x}_2^{\,2}}{\sigma_2^2}\right)}$$

Where

$$a(z) = \sqrt{\frac{1}{\sigma_1^2} z^2 + \frac{1}{\sigma_2^2}} \quad , \qquad b(z) = \frac{\bar{x}_1^{\,2}}{\sigma_1^2} z + \frac{\bar{x}_2^{\,2}}{\sigma_2^2}$$

$$c(z) = e^{\frac{1}{2}\frac{b^2(z)}{a^2(z)} - \frac{1}{2}\left(\frac{\bar{x}_1^{\,2}}{\sigma_1^2} + \frac{\bar{x}_2^{\,2}}{\sigma_2^2}\right)} \quad , \quad \Phi(z) = \int_{-\infty}^{z} \frac{1}{\sqrt{2\pi}} e^{-\frac{1}{2}u^2} \, du$$

where σ_1 is standard deviation of the incoming velocity, $\bar{x}_1$ is the mean of the incoming velocity, σ_2 is standard deviation of the rebounding velocity, $\bar{x}_2$ is the mean of the rebounding velocity, and z is the COR.

The resulting distribution from performing the ratio distribution on two independent variables is a Cauchy distribution. Since Cauchy distributions do not have a mathematically definable mean or standard deviation, these values are estimated based on the probability density function. These estimated mean and standard deviation values for e, e_N, e_T are presented for each of the test cases in the results section.

3.4 Literature Comparison

To confirm that the data reduction technique was accurate, a comparison to previous literature was made. Two trends from Tabakoff's [11, 12] study of fly ash impacts at ambient temperatures were compared to the ambient data taken in the current study. The trends for RENE 41, a nickel alloy, and AM 355, a stainless steel, were used. Figure 10 displays the plot of COR vs. angle of impact for the different metals. A similar trend is found between fly ash and ARD impacts. It should be noted that the impact speeds for the fly ash are 98 m/s which is much higher than the 28 m/s for the ARD. Although the fly ash has a different chemical composition and is much smaller in size, it has been included for a comparison. The comparison is very good with the difference in particle type and impact speed attributed to the change in COR.

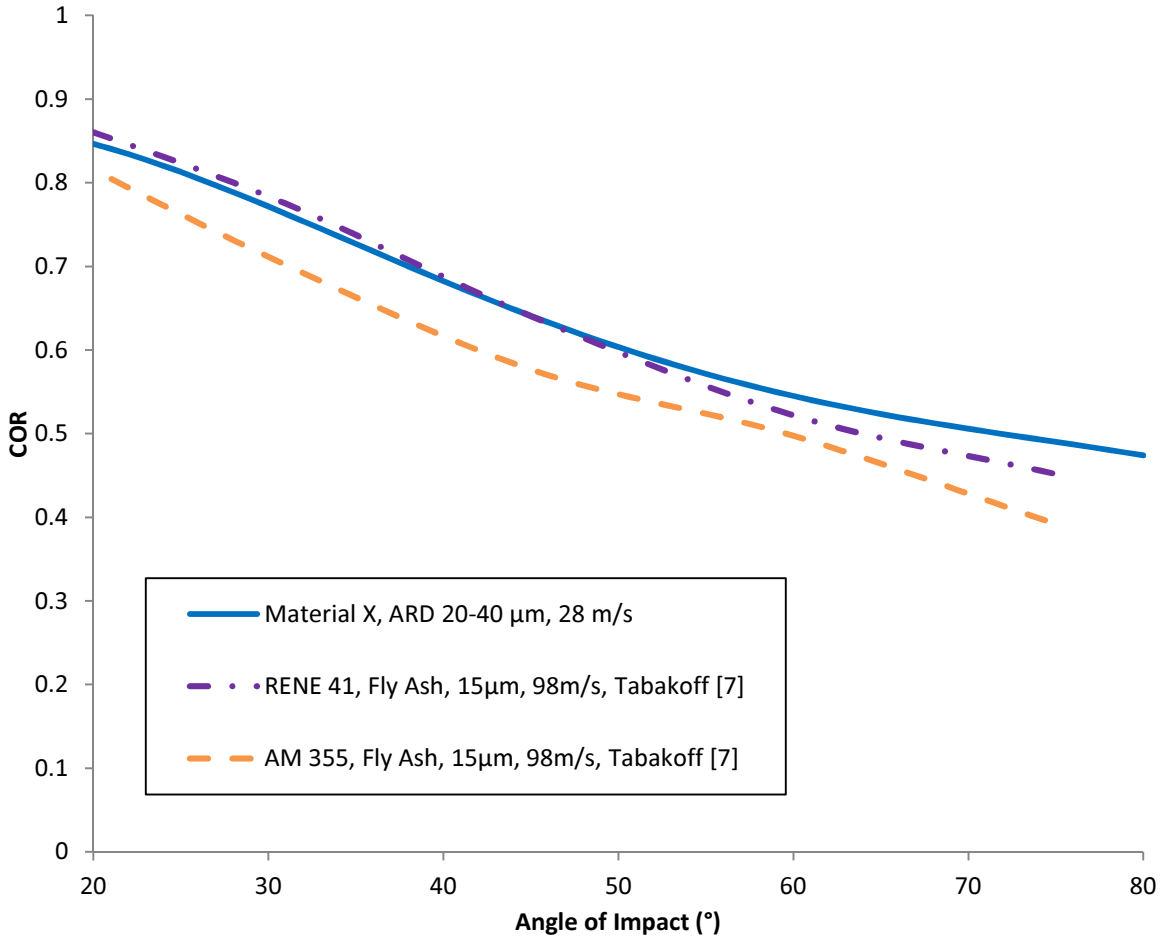

Figure 10. Plot of ambient COR vs. angle of impact comparison to literature

4 Results

4.1 Total Coefficient of Restitution at 28 m/s

The COR mean and standard deviation was calculated using the ratio distribution described previously. A fifth order polynomial was then fit to the COR data, where COR is a function of impact angle. The equation for the curve fit is displayed below as Equation 10. The coefficients for the equations of all the results can be found in Appendix A.

$$10) \quad e = a_5\beta^5 + a_4\beta^4 + a_3\beta^3 + a_2\beta^2 + a_1\beta + a_0$$

The impacts of 20-40μm ARD impacting the polished high temperature material were recorded for angles ranging from 30° to 80° for three different temperatures at 28 m/s. Figure 11 displays the sample mean for COR vs. angle of impact on the alloy for the three temperatures. The trends for COR are similar for the three temperatures. There is a decrease in COR as the temperature is increased from ambient, but at 1073 K the COR is higher than at 873 K. This increase in COR from 873 K to 1073 K is attributed to the formation of a chromium oxide layer on the alloy coupon at 1073 K. This oxide layer increases surface roughness and hardness which affects the COR. The average decrease in COR from ambient to 873 K is 1.8%. The average increase in COR from ambient to 1073 K is 10.2%.

There is a decrease in COR as the angle of impact is increased. There is more local deformation to the particle at higher angles of impact, due to the higher normal component of velocity. The irregular particle shapes increase the local deformation in the particle which causes a greater loss in momentum.

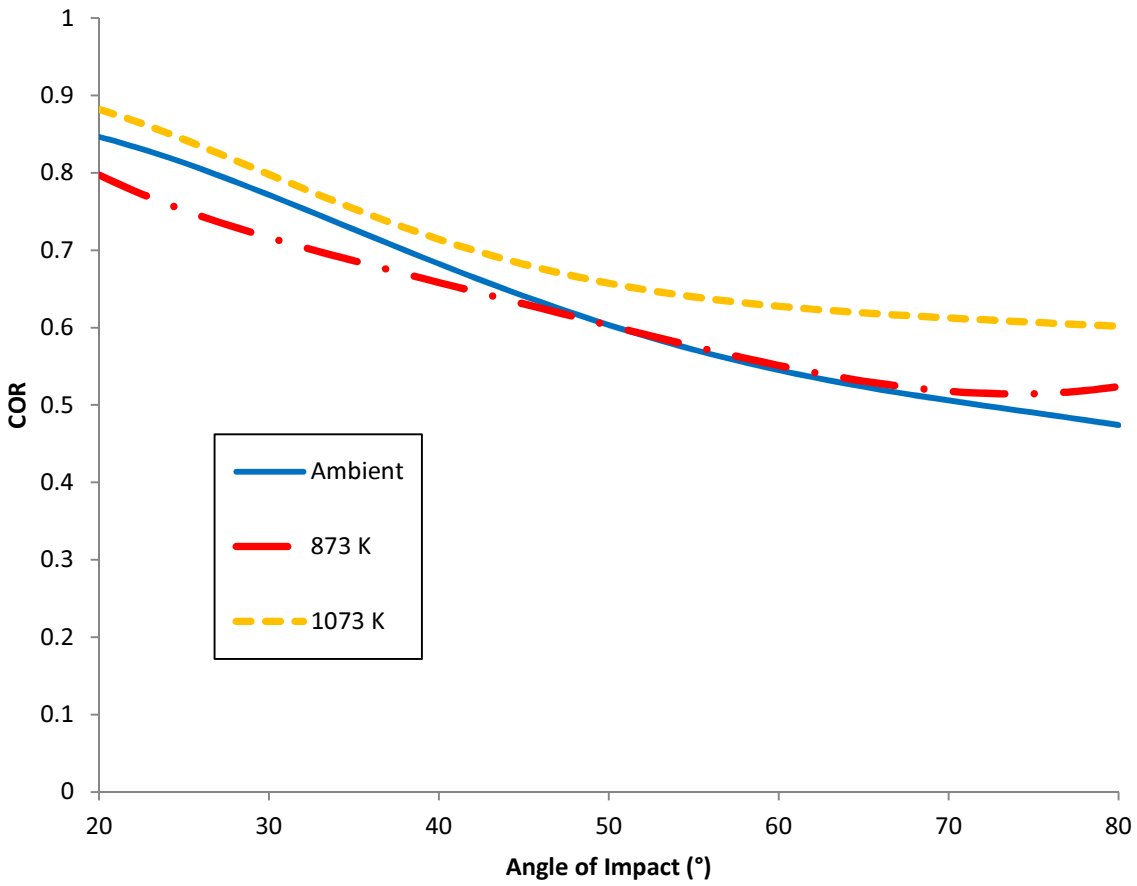

Figure 11. Plot of total COR vs. angle of impact at 28 m/s

Table 5 displays the estimated standard deviations for the sample mean for impact angles 30° to 80° at the three temperatures.

Table 5. Total COR Estimated Standard Deviation at 28 m/s

Mean COR Estimated Standard Deviation			
Angle	**Ambient**	**873 K**	**1073 K**
20	0.10	0.15	0.17
30	0.11	0.16	0.18
40	0.12	0.18	0.19
50	0.14	0.19	0.20
60	0.15	0.20	0.21
70	0.15	0.20	0.21
80	0.14	0.19	0.19

4.2 Normal Coefficient of Restitution at 28 m/s

Figure 12 displays the normal COR vs. angle for the three different temperatures at 28 m/s. It is believed that the formation of a chromium oxide layer, in addition to roughness due to erosion, increases the surface roughness of the coupon. This causes transfer of energy from the tangential to the normal direction due to the "shadow effect" noted by Sommerfeld and Huber[4]. The substantially higher normal COR observed between 20° and 40° angle of impact is believed to be due to this effect. At these low impact angles, the rebounding angle is higher than the impact angle. This increases the rebounding normal component of velocity causing an increase in the normal COR. It is also the reason that the normal COR is substantially higher for the high temperature cases as the surface roughness of these two cases is higher than the ambient case.

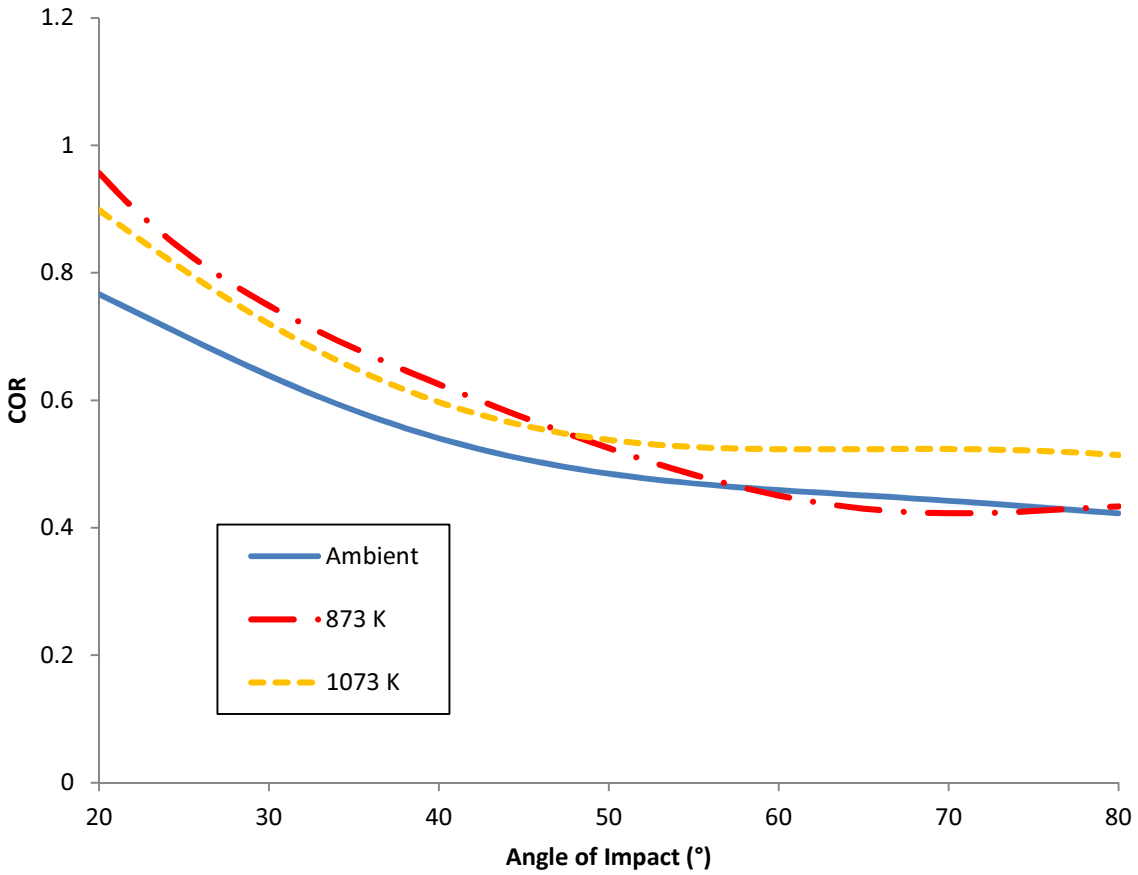

Figure 12. Plot of normal COR vs. angle of impact at 28 m/s

Table 6 displays the estimated standard deviations for the trends in Figure 12. The table shows that the shallow angles of impact have the highest deviation. It should be noted that the amount of velocity measured in the normal direction is very small for the data between 20° and 30°. At these low angles of impact the signal to noise ratio is very large causing more scatter in the COR data. This explains why the standard deviations at low angles of impact are much larger. Figure 13 displays of plot of the normal COR vs. angle of attack for the 873 K case with the standard deviations plotted. From the figure it is obvious that the standard deviation is twice as large at 20° than at 80°.

Table 6. Normal COR Estimated Standard Deviation at 28 m/s

Normal COR Estimated Standard Deviation			
Angle	**Ambient**	**873 K**	**1073 K**
20	0.33	0.41	0.40
30	0.23	0.29	0.30
40	0.19	0.24	0.26
50	0.17	0.21	0.24
60	0.16	0.19	0.22
70	0.15	0.19	0.19
80	0.14	0.19	0.17

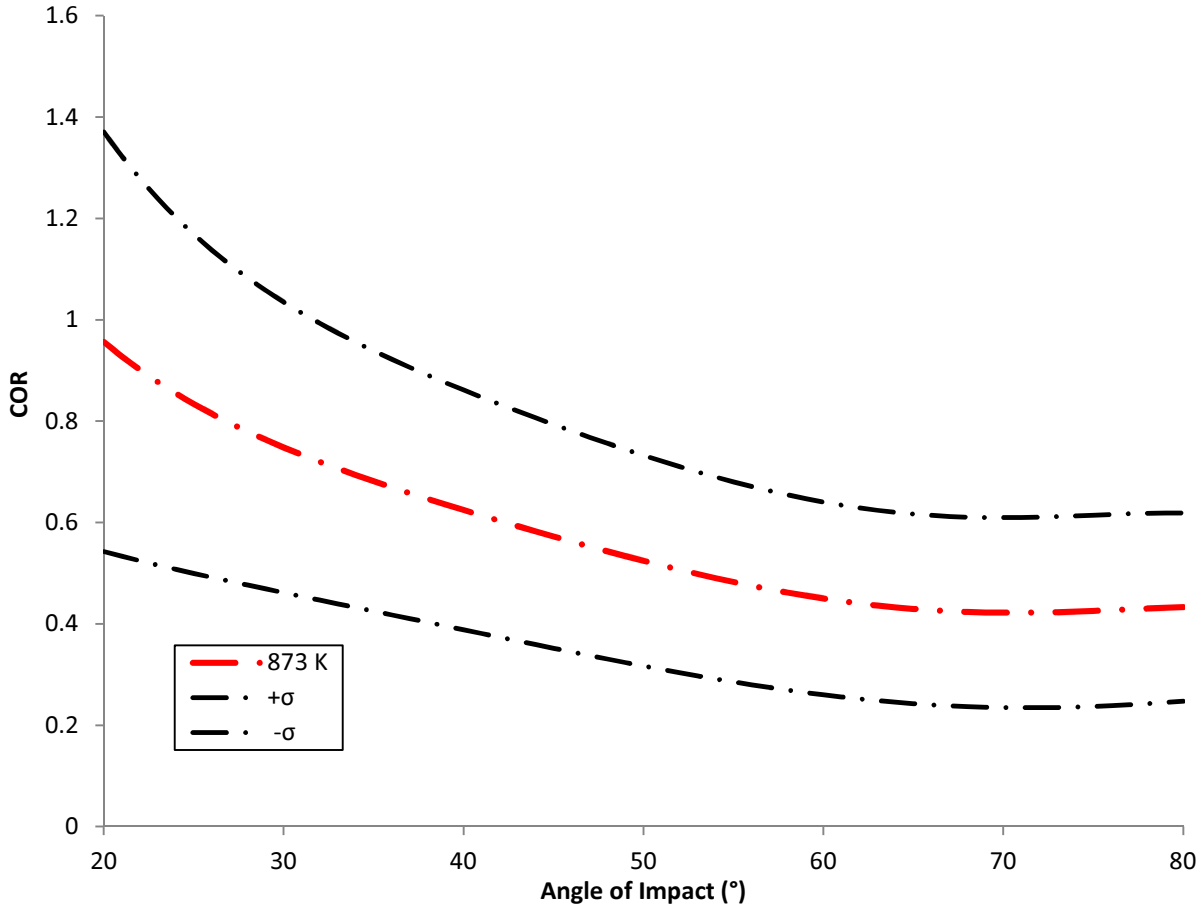

Figure 13. Plot of Normal COR for 873 K with Standard Deviations

4.3 Tangential Coefficient of Restitution at 28 m/s

Figure 14 displays the tangential COR vs. angle for the three different temperatures at 28 m/s. The trends for all temperatures are similar. There is a significant decrease in tangential COR from ambient to 873 K, but there is no decrease from ambient to 1073K. This increase in tangential COR from 873 K to 1073 K is attributed to the formation of a chromium oxide layer. There is a large amount of scatter in the data at angles of impact higher than 70°. There is also a steep rise in tangential COR at 80°. This is, in essence, the shadow effect [4] in reverse. There is a transfer of energy from the normal direction to the tangential direction. The increase in surface roughness causes the rebounding angle to be lower than the impact angle. This increases the rebounding tangential component of velocity causing an increase in the tangential COR.

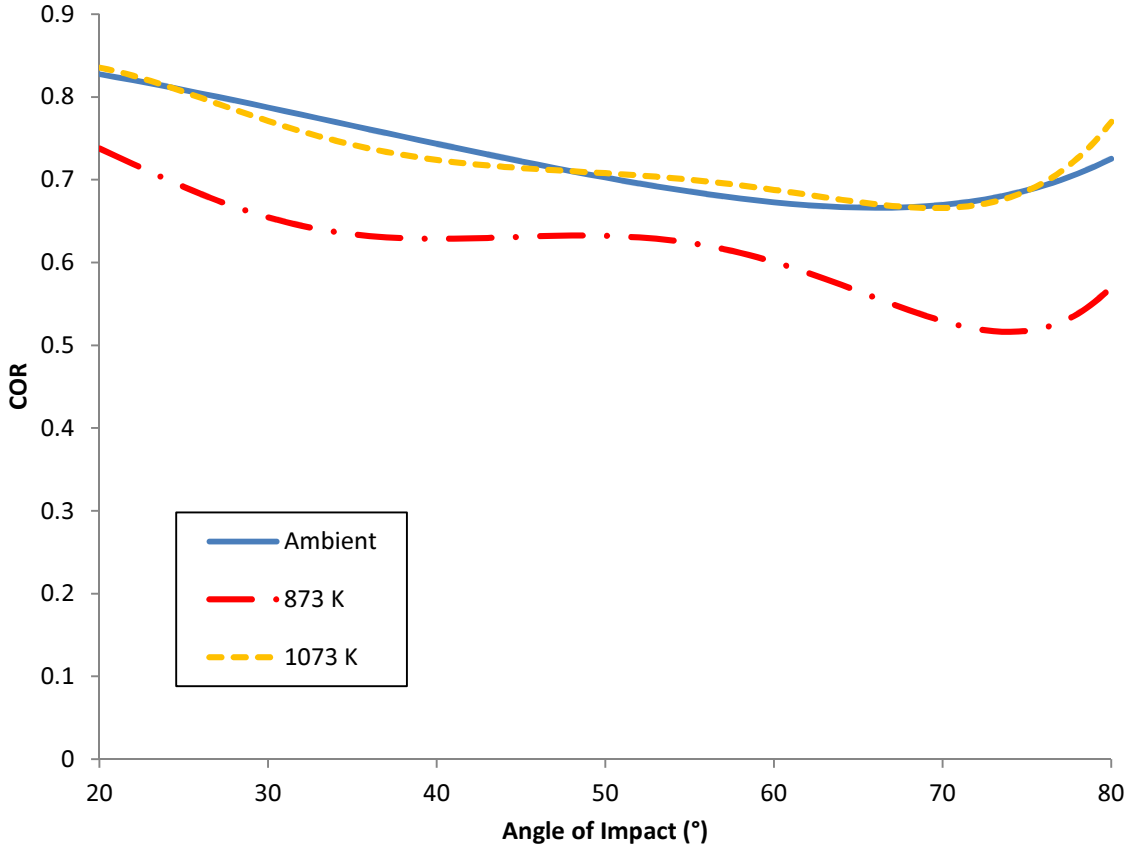

Figure 14. Plot of tangential COR vs. angle of impact at 28 m/s

Table 7 displays the estimated standard deviations for the trends in Figure 14. The table shows that the larger angles of impact have the highest deviation. One of the reasons for this is due to the small magnitude of the tangential velocity at these high angles of impact. This creates a very small signal which is then easily influenced by other factors. The surface roughness and particle irregularities can cause the particles to bounce at unexpected angles and have trajectories in unexpected directions. Any deviation of the rebound angle will cause substantial exchange on energy from the normal into the tangential direction. Since the effects of particle irregularities and surface roughness are essentially random, they cause a great increase in the scatter of the data at the very high angles of incidence.

Table 7. Tangential COR Estimated Standard Deviation at 28 m/s

Tangential COR Estimated Standard Deviation			
Angle	**Ambient**	**873 K**	**1073 K**
20	0.18	0.21	0.23
30	0.16	0.24	0.27
40	0.18	0.28	0.30
50	0.22	0.32	0.34
60	0.31	0.50	0.50
70	0.51	0.85	0.83
80	0.93	1.09	1.06

4.4 Total Coefficient of Restitution at 70 m/s

The impacts of 20-40μm ARD impacting the polished high temperature alloy were recorded for angles ranging from 30° to 80° for five different temperatures at 70 m/s. Figure 15 displays the sample mean for COR vs. angle of impact on the material for the five temperatures. The trends for COR are similar for the five temperatures. There is a decrease in COR as the impact angle increases, which has previously been explained.

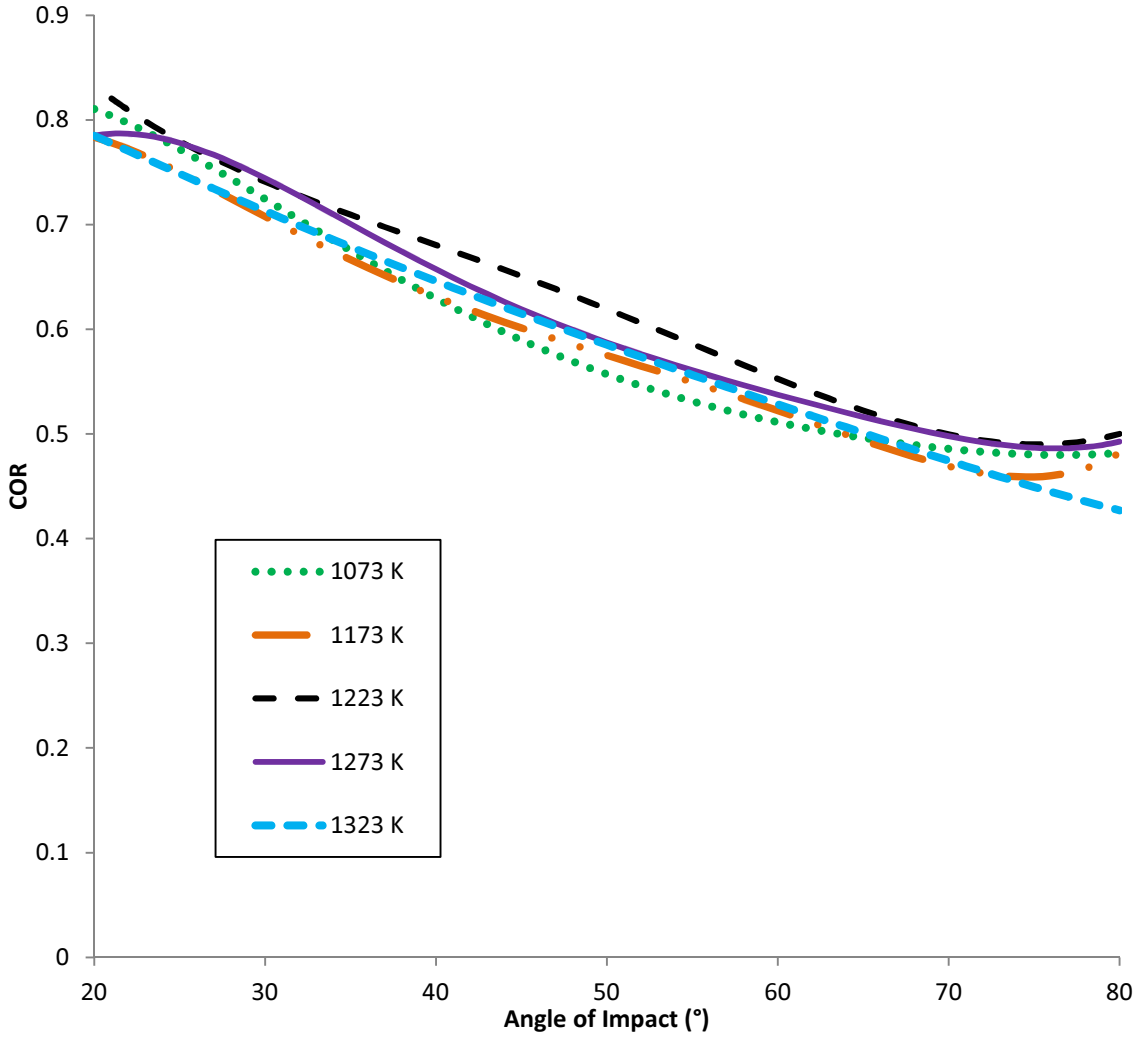

Figure 15. Plot of total COR vs. angle of impact at 70 m/s

Figure 16 displays the results for the 1073 K, 1173 K, and 1223 K cases only. The figure shows that there is a decrease in COR from the 1073 K to the 1173 K case. The average decrease in COR from 1073 K to 1173 K is 0.6%. The COR increased when the temperature was increased to 1223 K. The average increase in COR from 1073 K to 1223 K is 5.0%. The reason for the increase in COR at the 1223 K case is unknown. It is postulated that a material property change occurs at this temperature and hardens the surface of the coupon.

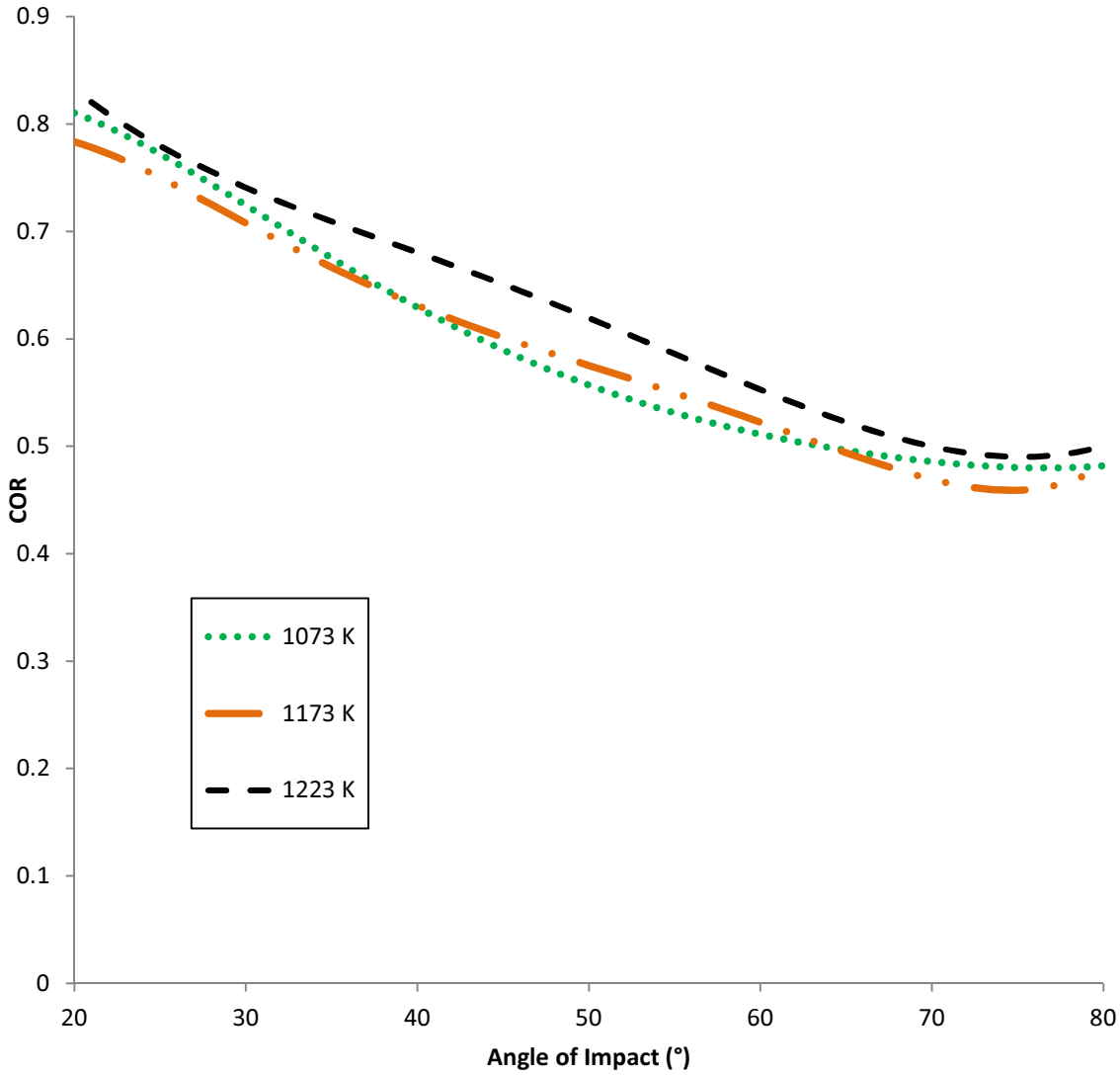

Figure 16. Plot of total COR vs. angle of impact at 70 m/s for select temperatures

Figure 17 displays the results for the 1223 K, 1273 K, and 1323 K cases only. The figure shows that there is a decrease in COR as temperature is increased. The average decrease in COR from 1223 K to 1273 K is 1.7%. The average decrease in COR from 1223 K to 1323 K is 4.7%.

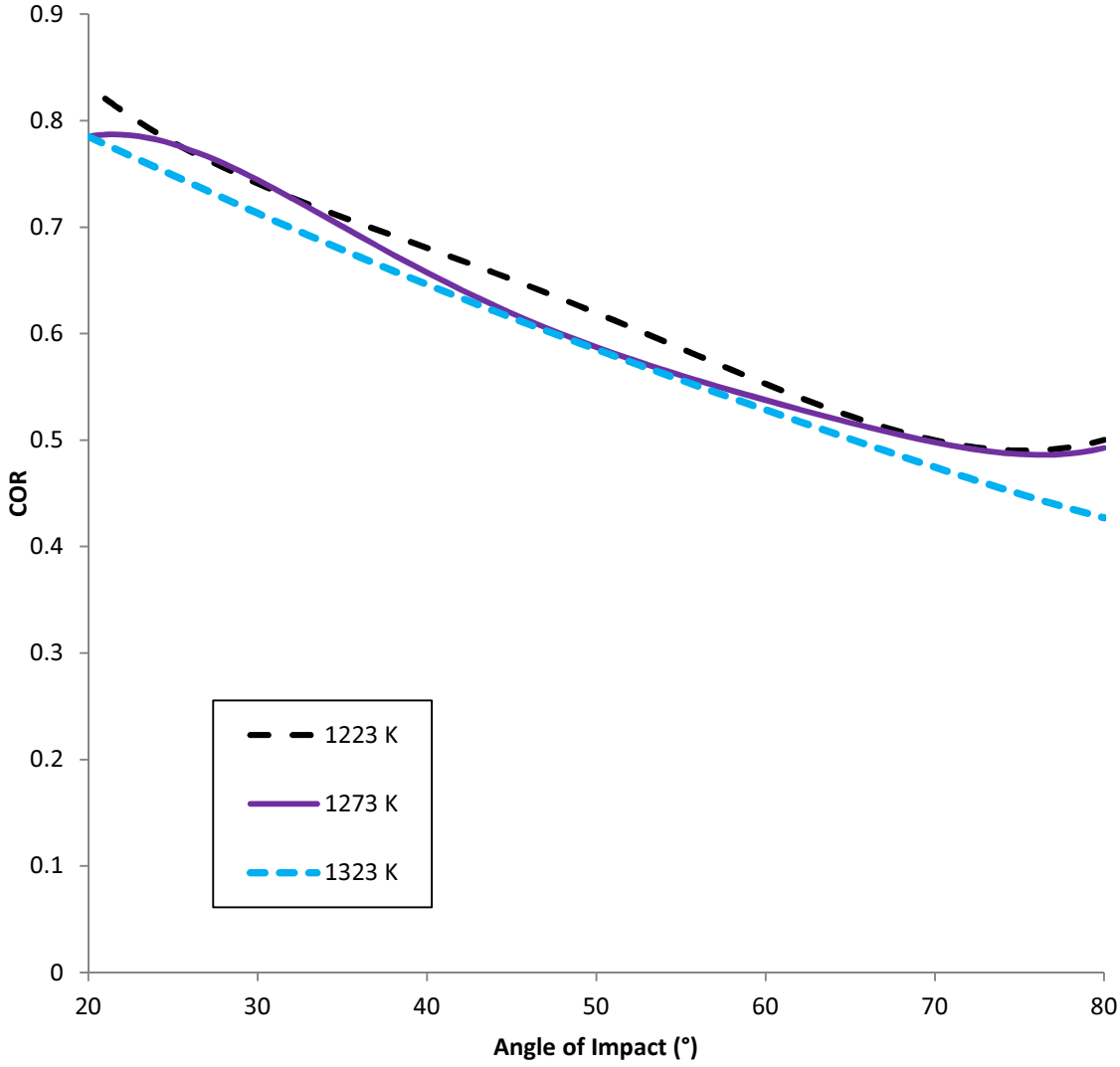

Figure 17. Plot of total COR vs. angle of impact at 70 m/s for select temperatures

It is important to understand that sand particles, especially microparticle sand, vary in composition from particle to particle. This means that some percentage of the particles will be fully molten at the temperatures tested in these experiments, while others

will retain most of their crystalline structure, and thus rebound from the target. While deposition was observed in the 1273 K and 1323 K cases, a substantial number of the particles retained enough of their solid state characteristic to rebound and be recorded by the experiment as a COR data point.

Table 8 displays the estimated standard deviations for the sample mean for impact angles 30° to 80° for the data at the five temperatures.

Table 8. Total COR Estimated Standard Deviation at 70 m/s

Mean COR Estimated Standard Deviation					
Angle	**1073 K**	**1173 K**	**1223 K**	**1273 K**	**1323 K**
20	0.10	0.09	0.13	0.11	0.15
30	0.10	0.10	0.13	0.14	0.13
40	0.12	0.11	0.16	0.15	0.15
50	0.13	0.13	0.19	0.17	0.18
60	0.15	0.15	0.21	0.20	0.21
70	0.17	0.16	0.22	0.22	0.22
80	0.16	0.15	0.22	0.21	0.17

4.5 Normal Coefficient of Restitution at 70 m/s

Figure 18. Plot of normal COR vs. angle of impact at 70 m/s displays the normal COR vs. angle for the different temperatures. As impact angle increases, normal COR decreases. As described in section 4.2, this causes transfer of energy from the macroscopic tangential to the macroscopic normal direction due to the "shadow effect" noted by Sommerfeld and Huber [4]. This shadow effect simply is the biasing effect of particles impacting on only one side of any surface roughness peaks. The higher COR observed between 20° and 40° angle of impact is believed to be due to this effect. Below 30° angle of impact the data crosses due to the nature of the curve fits. There seems to be no correlation between normal COR and temperature for this material at 70 m/s.

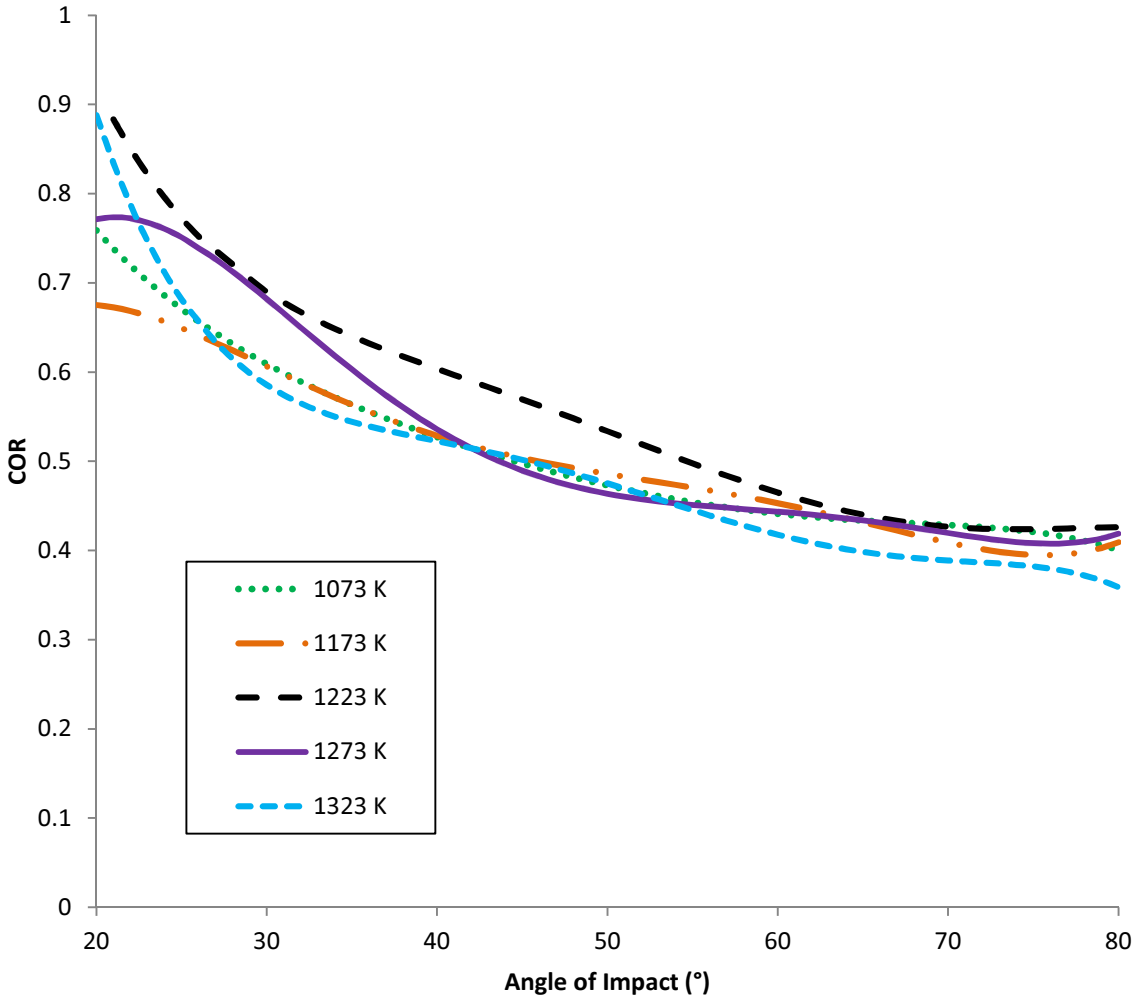

Figure 18. Plot of normal COR vs. angle of impact at 70 m/s

Table 9 displays the estimated standard deviations for the normal COR at the different temperatures. The table shows that the shallow angles of impact have the highest deviation. As described in section 4.2, it should be noted that the amount of velocity measured in the normal direction is very small for the data between 20° and 30°. This makes the signal to noise ratio large and explains why the standard deviations at low angles of impact are much larger.

Table 9. Normal COR Estimated Standard Deviation at 70 m/s

Normal COR Estimated Standard Deviation					
Angle	**1073 K**	**1173 K**	**1223 K**	**1273 K**	**1323 K**
20	0.31	0.30	0.57	0.43	0.62
30	0.25	0.24	0.32	0.35	0.28
40	0.19	0.19	0.27	0.27	0.24
50	0.17	0.17	0.25	0.22	0.23
60	0.17	0.17	0.21	0.21	0.20
70	0.16	0.16	0.21	0.21	0.20
80	0.16	0.15	0.19	0.18	0.15

4.6 Tangential Coefficient of Restitution at 70 m/s

Figure 19 displays the tangential COR vs. angle for the different temperatures at 70 m/s. The trends for all temperatures are similar. Generally, the tangential COR decreases as temperature increases. There are increases in tangential COR from 20° to 30°, 50° to 60°, and 70° to 80°. The first two are due to the nature of the fifth order curve fits applied to the raw data. The steep rise in tangential COR at 80° is caused by the shadow effect [4] in reverse. The increase in surface roughness causes the rebounding angle to be lower than the impact angle, thus increasing the rebounding tangential component of velocity and tangential COR.

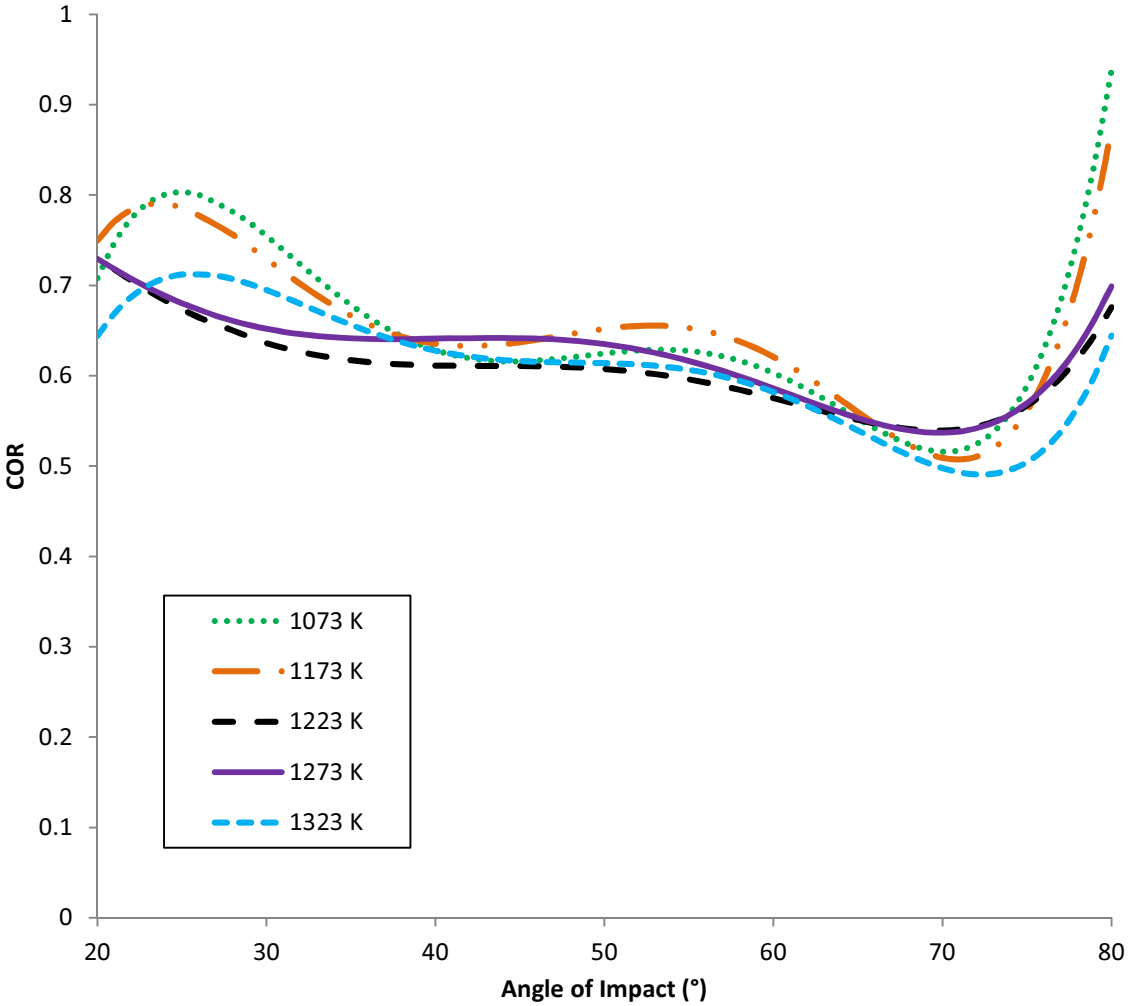

Figure 19. Plot of tangential COR vs. angle of impact at 70 m/s

Table 10 displays the estimated standard deviations for the tangential COR at the different temperatures. The table shows that the larger angles of impact have the highest deviation. One of the reasons for this is due to the small magnitude of the tangential velocity at these high angles of impact. Unlike at small angles where effects of surface roughness and particle irregularities bias the COR, at high angles the effects are essential random and a lead to an extremely large increase in standard deviation

Table 10. Tangential COR Estimated Standard Deviation at 70 m/s

Tangential COR Estimated Standard Deviation					
Angle	**1073 K**	**1173 K**	**1223 K**	**1273 K**	**1323 K**
20	0.21	0.10	0.29	0.23	0.35
30	0.15	0.16	0.26	0.31	0.25
40	0.19	0.18	0.28	0.31	0.29
50	0.24	0.22	0.36	0.33	0.36
60	0.33	0.33	0.48	0.44	0.50
70	0.55	0.56	0.69	0.71	0.74
80	1.13	1.13	1.19	1.17	1.06

5 Discussion of Results

5.1 Effect of Temperature on COR

Figure 20 displays a plot of COR vs. temperature for three different impact angles at ambient, 873 K, and 1073 K. The COR decreases at 30° from ambient to 873 K and stays the same at 50° and 70°. There is a jump in COR from 873 K to 1073 K. This is caused by the formation of an oxide layer. This oxide layer increases the surface hardness of the coupon which increases the COR. Harder surfaces do not deform as easily as softer surfaces, so less kinetic energy is lost in the impact.

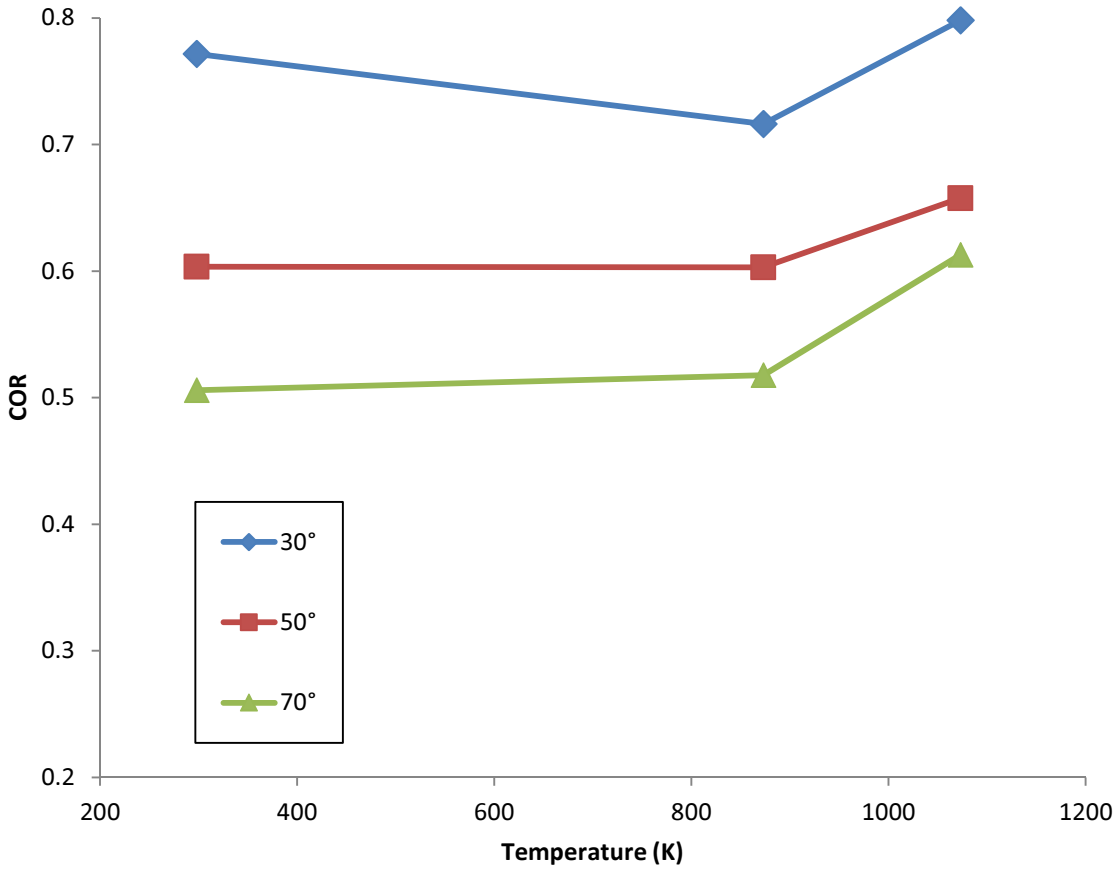

Figure 20. Plot of COR vs. temperature for different impact angles at 28 m/s

Figure 21 displays a plot of COR vs. temperature for three different impact angles at 1073 K, 1173 K, 1223 K, 1273 K, and 1323 K. There is a slight decrease in COR from 1073 K to 1173 K at 30° and 70°, but a slight increase at 50°. There is a jump in COR from 1173 K to 1223 K, likely caused an increased thickness in the oxide layer. The COR decreases with increasing temperature for all angles of impact from 1223 K to 1323 K.

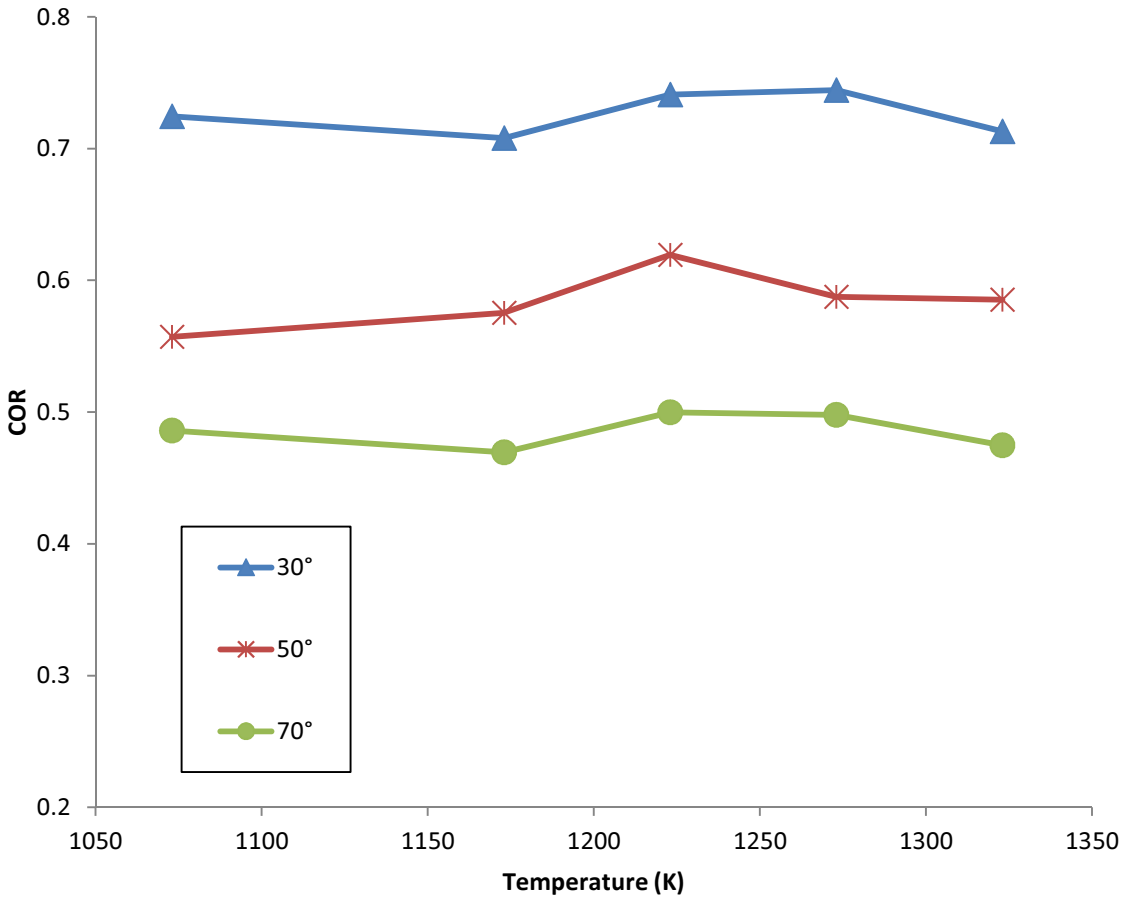

Figure 21. Plot of COR vs. temperature for different impact angles at 70 m/s

5.2 Effects of Temperature and Impingement Angle on Deposition

Images were taken, using an Axiovert 200M optical microscope, of the sand deposition on the surface of the coupon after testing at 1273K and 1323K. Figure 22-Figure 27 show pictures of the coupon after particles impacted at 40°, 50°, and 70°. The images were taken at an optical magnification of 100X. Many of the particles that appear in the image are out of focus. This is due to the very narrow range of focus which allows the surface and smaller particles to be in focus while the tops of much larger particles are substantially out of focus. The same amount of ARD was injected into the flow for each test, 60 g.

The temperature of the flow has a large effect on the amount of deposition. Figure 22 and Figure 23 display pictures of the coupon at 40° for 1273 K and 1323 K, respectively. Deposition began at 1273 K. This indicates that 1273 K is a critical temperature for ARD causing some of the particles to become molten at this temperature and deposit. Figure 24 and Figure 25 display images of the coupon at 50°. Figure 25 and Figure 26 display images of the coupon at 70°. There are substantially more deposited particles on the 1323 K coupon. The same trend is observed at all angles of impact. As the temperature of the flow increases, a higher percentage of the particles become molten. There are irregularities in particle composition making the melting temperature different for each particle. When the particle's temperature approaches the glass transition temperature, the particle starts to soften and become molten. Softer particles take less energy to deform and subsequently are more likely to deposit.

The angle of impact also has a large effect on the amount of deposition observed. For both temperatures, there are substantially fewer deposited particles at the lower angles of impact. Even when effects of the projected area of the coupon normal to the flow are taken into account there are substantially more particles which deposit on the surface at 70° than 50° and slightly more at 50° than at 40°. Although not presented here this trend was observed at all angles of impact examined with the microscope. This is due to the magnitude of the normal velocity with which the particles strike the surface.

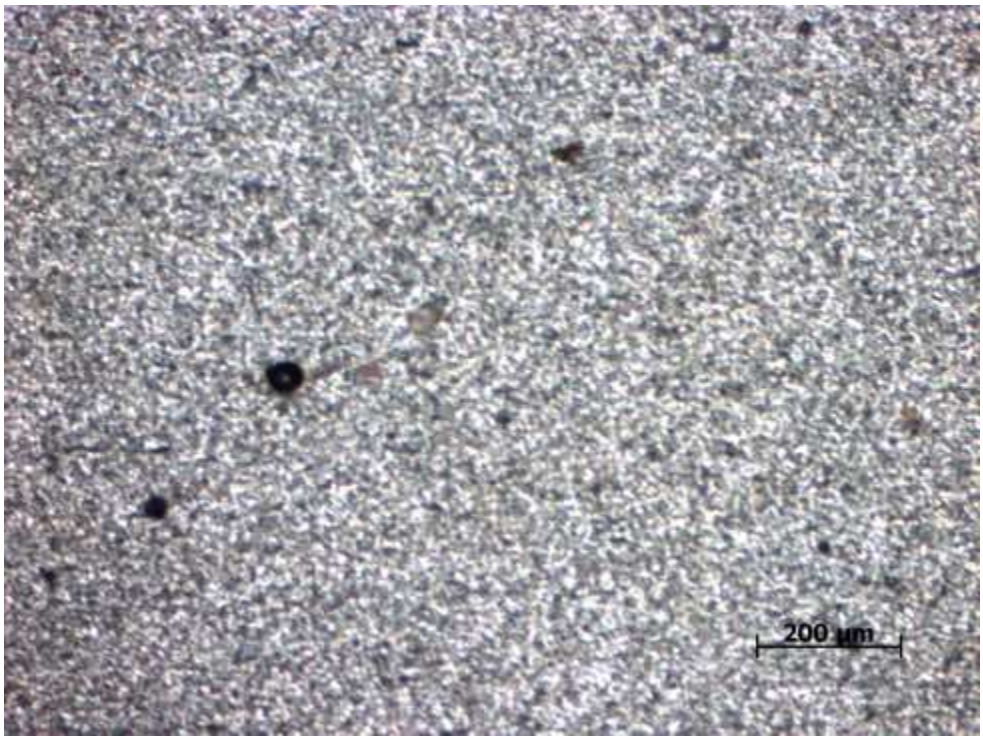

Figure 22. Sand deposition at 40° impact angle and 1273 K

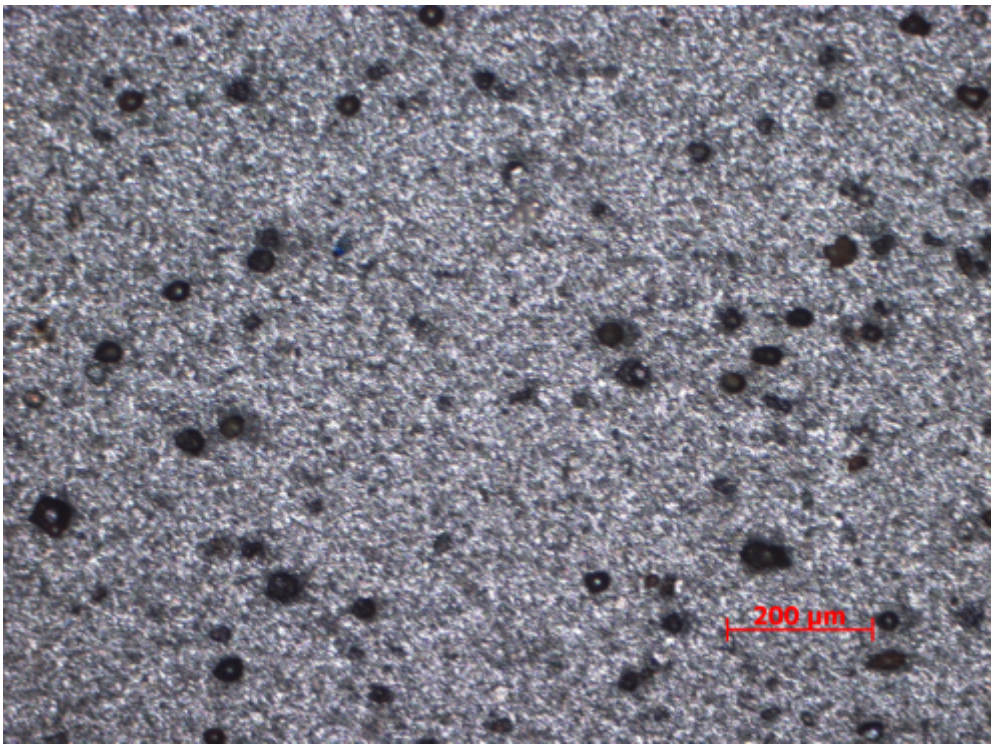

Figure 23. Sand deposition at 40° impact angle and 1323 K

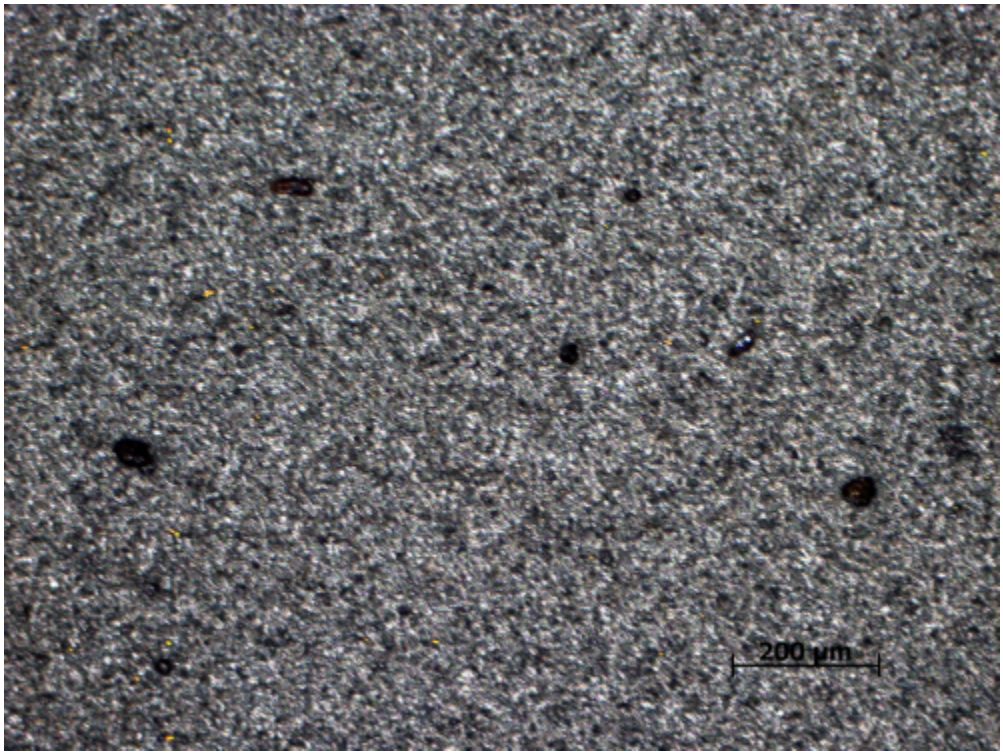

Figure 24. Sand deposition at 50° impact angle and 1273 K

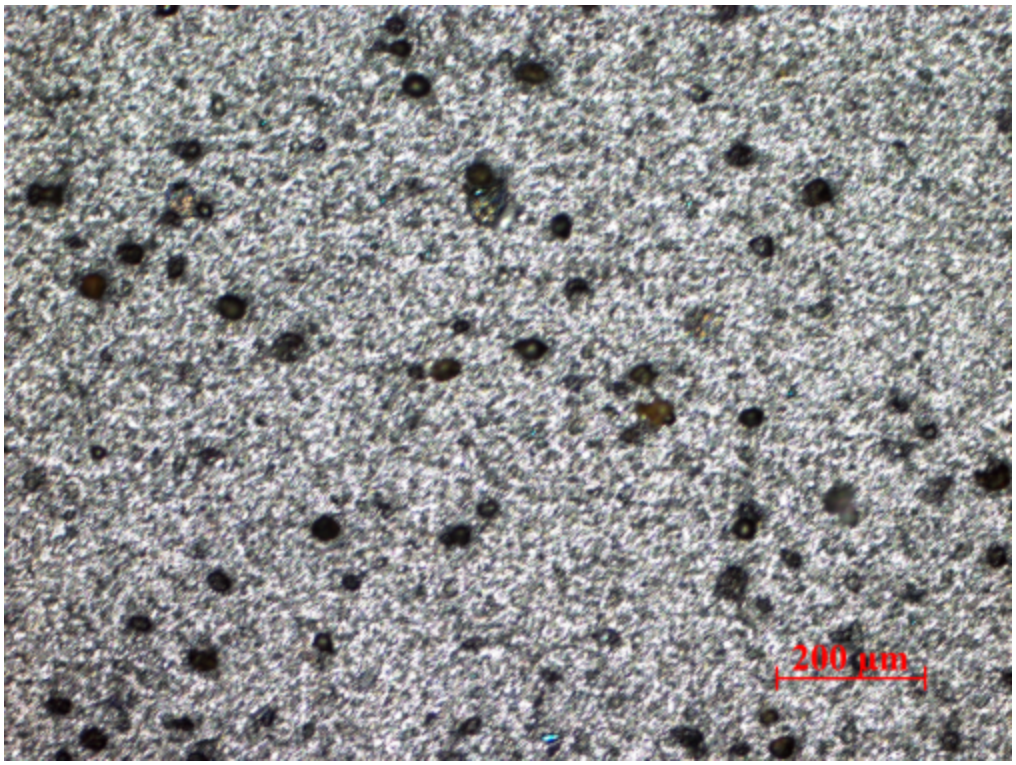

Figure 25. Sand deposition at 50° impact angle and 1323 K

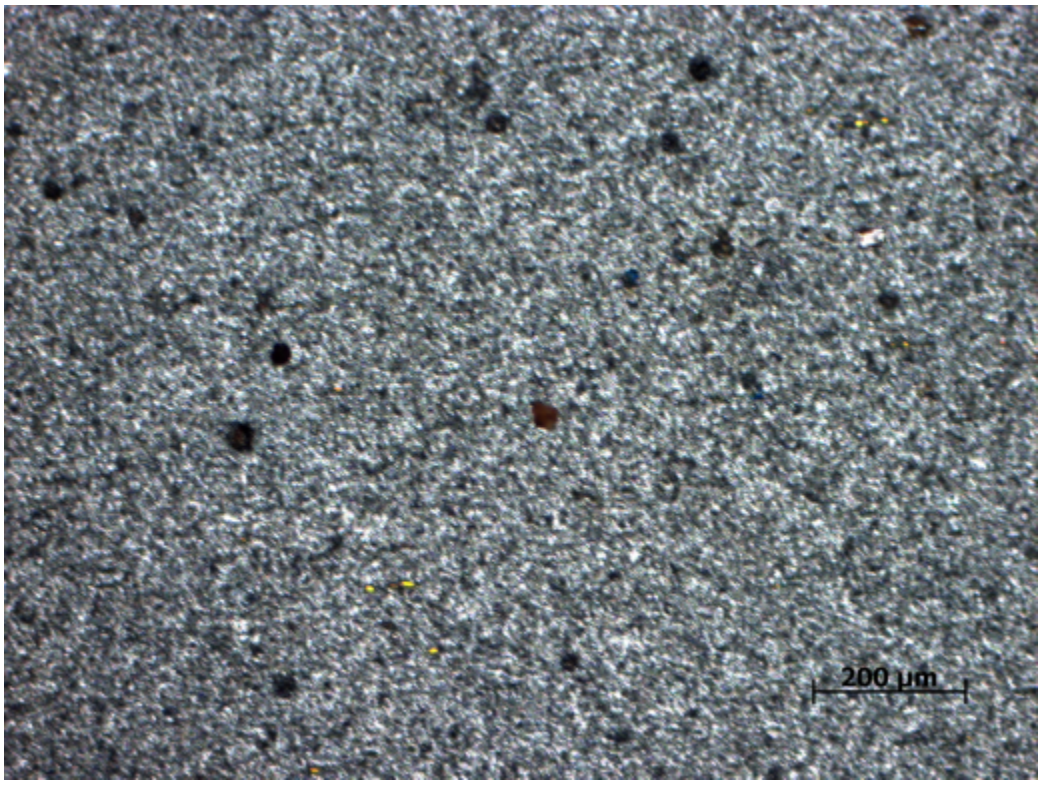

Figure 26. Sand deposition at 70° impact angle and 1273 K

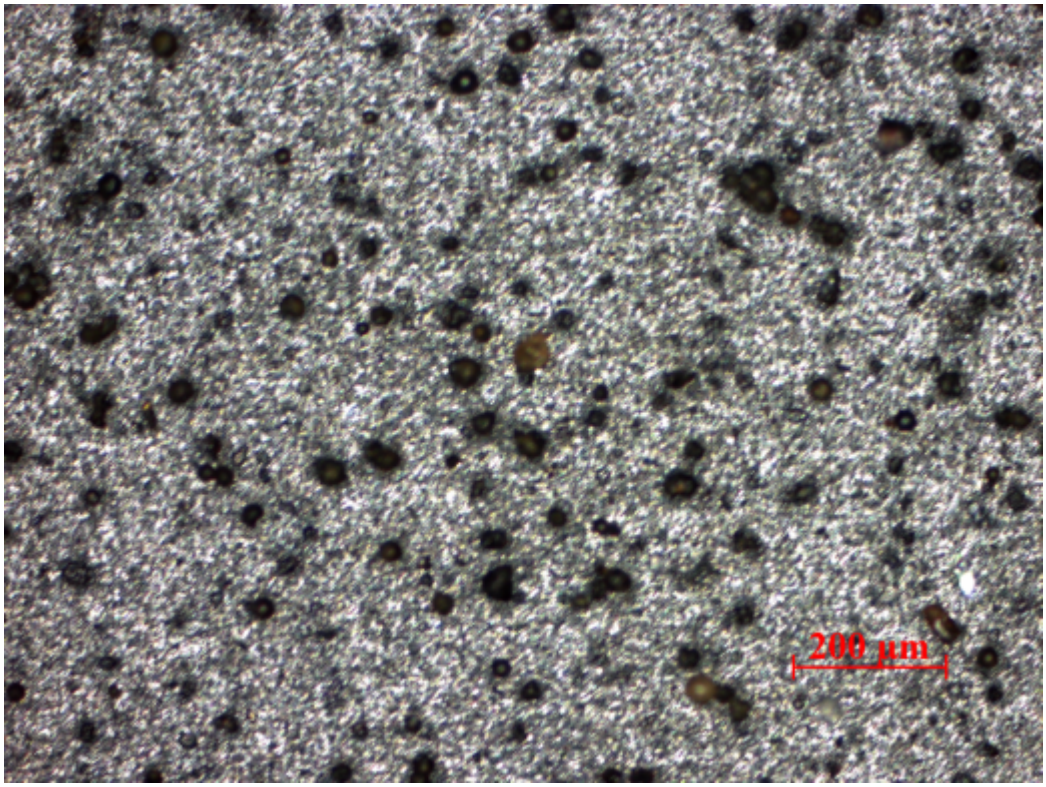

Figure 27. Sand deposition at 70° impact angle and 1323 K

Table 11 below displays the number of deposited particles for each temperature and angle of impact. An image processing code developed in MATLAB was used to analyze the images. There is a large increase in the number of deposited particles as temperature impact angle is increased. At 40° there are 9.6 times as many deposited particles at 1323 K than 1273 K. Similarly, at 50° there are 7.4 times as many deposited particles and at 70° there are 8.19 times as many deposited particles at 1323 K than 1273 K. This increase in deposition is due to the higher percentage of particles that become softer at higher temperatures causing them to deposit. Almost 3 times as many particles deposit at 70° than at 40°. This increase is due to the higher normal velocity that the particles have at 70°.

Table 11. Amount of Deposited Particles

Impact Angle (°)	Temperature (K)	Number of Deposited Particles
40	1273	7
40	1323	67
50	1273	10
50	1323	74
70	1273	21
70	1323	172

5.3 Comparison to Previous VT Aerothermal Rig Experiments

Previous experiments had been done on the high temperature material with an uncontrolled mass flow rate. The results have not been published and were performed by Colin Reagle and Jacob Delimont. Figure 28 displays a plot of the total COR vs. angle of impact for ambient, 873 K, and 1073 K all at different velocities. The results from Figure 28 are very similar to those in Figure 11. It needs to be noted that the results in Figure 28 were calculated using the old data reduction technique. Since these experiments, several major updates have been made to the data reduction technique (see Section 3). The data that is outputted from these two programs is different, but still comparable.

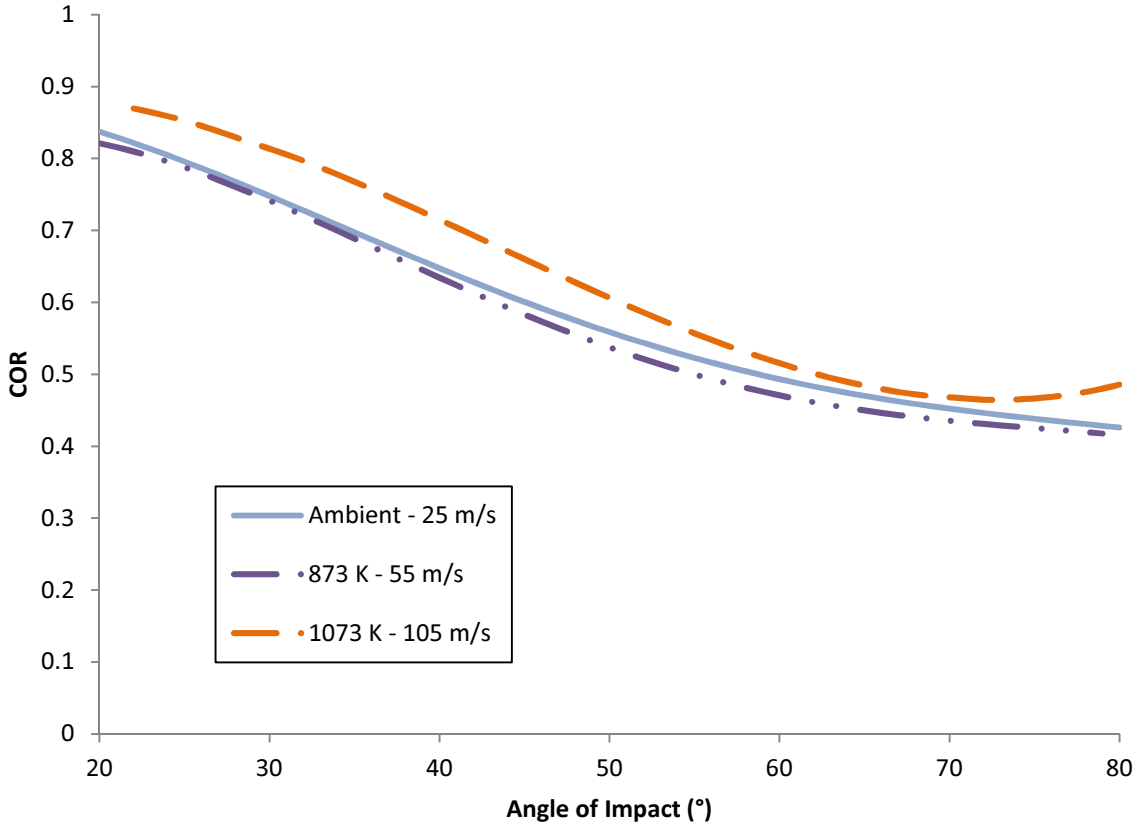

Figure 28. Plot of total COR vs. angle of impact from previous experiments

Figures 29 and 30 display plots of total COR vs. angle of impact for different velocities at 873 K and 1073 K, respectively. From Tabakoff's study [2] COR was found to decrease with increasing velocity. This result is confirmed in the figures below. The decrease in COR with increasing velocity is attributed to the increase in particle and wall deformation. Figure 29 displays two trends for velocities of 28 m/s and 77 m/s at a constant 873 K. As expected there is an overall decrease in COR as the velocity is increased. The different data reduction techniques used account for the higher COR at 77 m/s from 20° to 40°. Figure 30 displays three trends for velocities of 28 m/s, 70 m/s, and 105 m/s at 1073 K. There is a significant drop in COR from 28 m/s to 70 m/s of 14.4%. The 105 m/s data was calculated using the old data reduction technique, causing it to not follow the same trend.

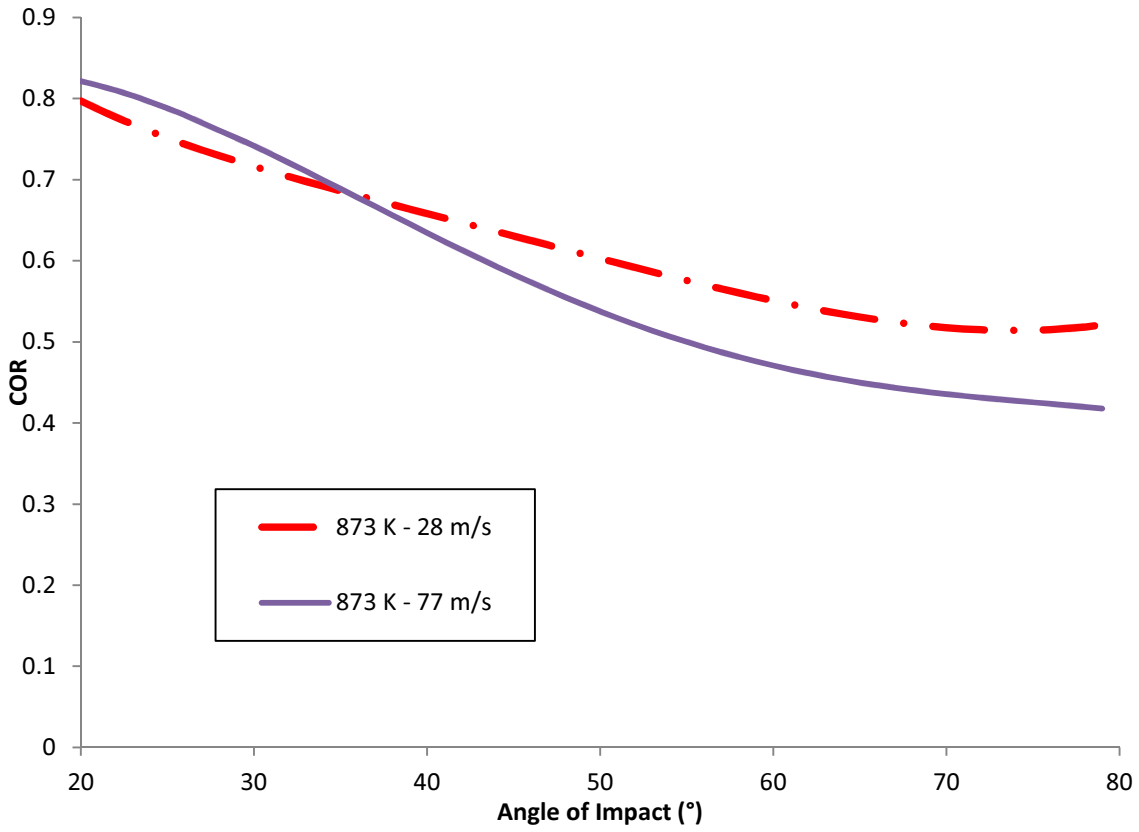

Figure 29. Comparison of 873 K total COR at different velocities

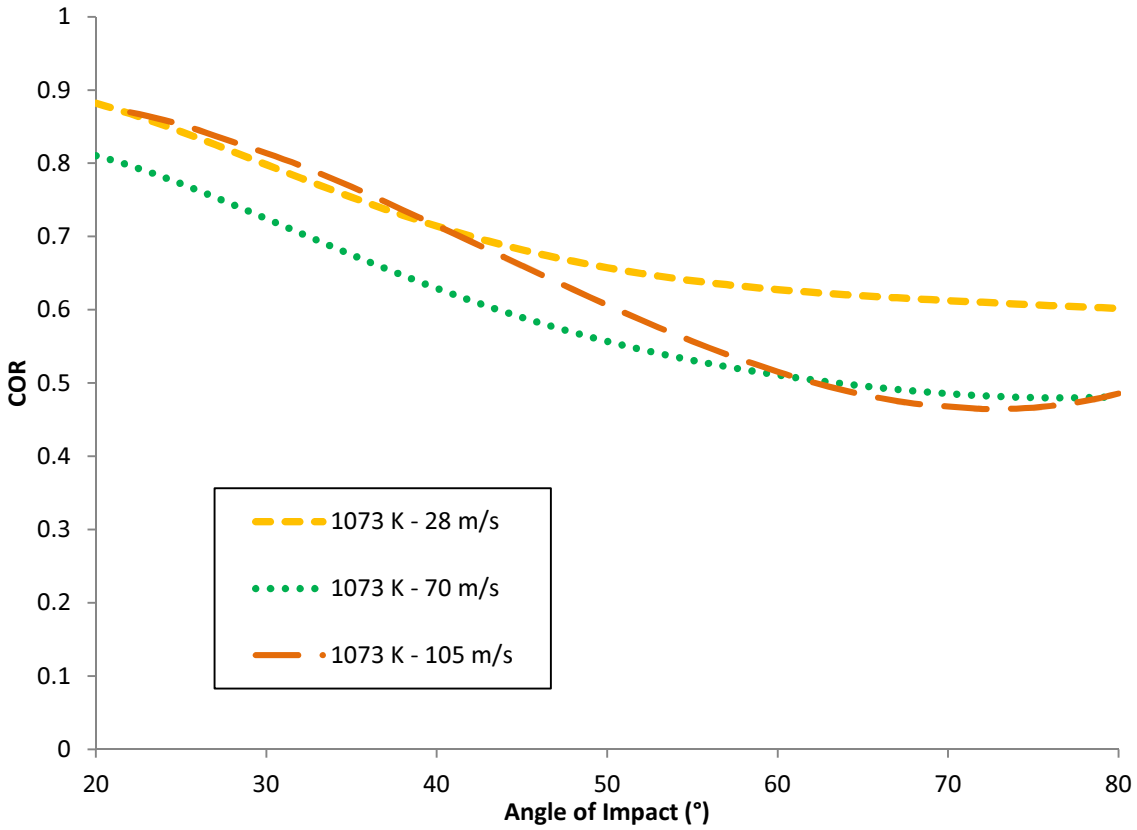

Figure 30. Comparison of 1073 K total COR at different velocities

6 Conclusions

6.1 Review of Experiment

The COR is a measure of a particle/wall collision and is used to study erosion and deposition. This study was conducted to observe the effect of temperature on COR of microparticle sand at a constant impact velocity. ARD of size 20-40μm were used in this study. COR was measure on a polished high temperature material coupon at several different conditions. The coupon was tested with a constant velocity of 28 m/s at temperatures of ambient, 873 K, and 1073 K. The coupon was also tested at a constant velocity of 70 m/s at temperatures of 1073 K, 1173 K, 1223K, 1273 K, and 1323 K. The angle of impact was varied from 30° to 80°. The Virginia Tech Aerothermal Rig was used to conduct all the testing outlined in this report. Modifications to the VT Aerothermal Rig were made to independently control velocity and temperature since the previous study by Reagle and Delimont [11, 12].

To measure the effects of temperature on COR, a laser camera particle tracking method was used. A Litron Nd:YAG laser is used to illuminate the particles in the test section. A monochrome Dantec Dynamics® FlowSense camera equipped with a Zeiss® Makro-Planar 2/50 lens is used to take images of the test section. An image pair is taken to track the particle's motion. The time between images is set to 15μs when testing at 28 m/s, and 6μs when testing at 70 m/s. These times allow the particles to move up to ~9 pixels between images, which is enough distance to get an accurate measure of the particle's velocity.

A data reduction method was established to handle this unique data. The Particle Tracking Velocimetry (PTV) method implements a band pass filter on the image to remove large objects. It then locates the particles and uses a radius of gyration calculation to find the particle centroid. After the particle locations have been determined, the particles are then correlated between the image pair to determine particle velocity. Once the particle velocity has been measured, the velocity is used as an initial condition for a Lagrangian particle tracking algorithm which uses a flow field calculated from ANSYS CFX for the Eulerian phase of the calculation.

After the particles velocity has been determined the COR is calculated. In order to determine the COR, incoming and rebounding particles are sorted into bins by the location of impact on the target coupon. A mean velocity of incoming particles as well as a mean of the rebounding particles at each location is then calculated. To calculate the distribution of the COR about the mean a ratio distribution is performed. A distribution derived by Hinkley [18] is used to calculate the COR. This more accurate method of calculating COR variation has not been used in previous studies.

6.2 Summary of Results

The impacts of 20-40μm ARD impacting the polished high temperature material were recorded for angles ranging from 30° to 80° for three different temperatures at 28 m/s and five different temperatures at 70 m/s. It was found in general COR decreases with increasing temperature only if the surface of the coupon does not change. In several of the tests, it was concluded that a hard oxide layer formed on the surface of the coupon at a certain temperature. This oxide layer increased the surface hardness of the coupon which increases the COR and causes the data to be shifted. It was also found that as velocity increases the COR decreases, even at elevated temperatures.

The main mechanism for energy loss in the impact was plastic deformation. The force of the impact causes compression of the crystal structure, which deforms the particle. As temperature increases, the atoms spread out due to the increased energy lowering the bond strength. Less energy is need to overcome the bonds and deform the particle, so COR is reduced at higher temperatures.

The effects of temperature and impact angle on deposition were studied. Images were taken of the sand deposition on the surface of the coupon after testing at 1273K and 1323K. The temperature of the flow has a large effect on the amount of deposition. There are substantially more deposited particles on the 1323 K coupon than the 1273 K coupon. This indicates that 1323 K is a critical temperature for ARD causing more of the particles to become molten at this temperature at deposit. The same trend is observed at all angles of impact. The same amount of ARD was injected into the flow for each test.

The angle of impact also has a large effect on the amount of deposition observed. For both temperatures, there are substantially fewer deposited particles at the lower angles of impact. Even when effects of the projected area of the coupon normal to the flow are taken into account there are substantially more particles which deposit on the surface at 70° than at 50° or 40°.

It was predicted that when deposition was observed the COR would decrease dramatically. Even though deposition occurs at 1273 K and 1323 K it is certain from the COR results that a large portion of the particles are still rebounding from the target coupon while some particles are depositing.

6.3 Suggestions for Further Investigations

Studying the COR of microparticle sand at near melting temperatures has not been presented in open literature. There is plenty of future work to be done to help understand the fundamentals of particle/wall interactions at near melting temperatures.

The coupon temperature in this research was always lower than the flow. This temperature difference allows the particles to cool after impact and deposit. Heating the coupon to temperatures at or above the temperature of the flow may produce interesting results. If the temperature of the coupon is above the flow temperature, particles may not deposit because they will not solidify. This would drastically change the amount of deposition observed at the near melting temperatures. Contrary to heating the coupon, cooling the coupon would also produce interesting results.

Other possibilities include testing with different materials used in the gas turbine industry. Varying the velocity of the flow to study its effects on COR would provide interesting results. Changing the type and size of particles to study these effects on COR would also provide good research.

Finally, for further investigation a rebound ratio should be incorporated into the calculation of the COR. This will take into account the particles that deposit, but are discarded from the current data reduction method. Incorporating the rebound ratio will improve the quality of the results and better predict when deposition will occur.

7 References

[1] Goldsmith, W., 2002, Impact : the theory and physical behaviour of colliding solids, Dover Publications, Mineola, N.Y.

[2] Tabakoff, W., Grant, G., and Ball, R., 1974, "An Experimental Investigation of Certain Aerodynamic Effects on Erosion," AIAA-74-639.

[3] Li, X., Dunn, P.F., and Brach, R.M., 2000, "Experimental and Numerical Studies of Microsphere Oblique Impact with Planar Surfaces," Aerosol Science and Technology, 31(5), pp. 583-594.

[4] Sommerfeld, M., and Huber, N., 1999, "Experimental analysis and modelling of particle-wall collisions," International Journal of Multiphase Flow, 25, pp. 1457-1489.

[5] Mok, C. H., and Duffy, J., 1964, "The Behaviour of Metals at Elevated Temperatures Under Impact with a Bouncing Ball," Int J Mech Sci, 6, pp. 161-175.

[6] Brenner, S. S., Wriedt, H. A., and Oriani, R. A., 1981, "Impact adhesion of iron at elevated temperatures," Wear, 68(2), pp. 169-190.

[7] Tabakoff, W., 1991, "Measurements of Particles Rebound Characteristics on Materials Used in Gas Turbines," J. of Propulsion and Power, 7(5), pp. 805-813.

[8] Tabakoff. W, H., A., and Murugan, D.M, 1996, "Effect of Target Materials on the Particle Restitution Characteristics for Turbomachinery Application," J. of Propulsion and Power, 12(2), pp. 260-266.

[9] Wakeman, T., and Tabakoff, W., 1979, "Erosion Behavior in a Simulated Jet Engine Environment," J. Aircraft, 16(12), pp. 828-833.

[10] Hamad A., T. W., "Experimental and Numerical Simulation of the Effects of Ingested Particles in Gas Turbine Engines," Proc. AGARD, NATO.

[11] Reagle C., D. J., Ng W., Ekkad S., Rajendran V., 2013, "Measuring the coefficient of restitution of high speed microparticle impacts using a PTV and CFD hybrid technique," Measurement Science and Technology, 24(10).

[12] Reagle CJ, D. J., Ng WF, Ekkad SV, 2014, "Study of Microparticle Rebound Characteristics Under High Temperature Conditions," Journal of Engineering for Gas Turbines and Power, 136(1).

[13] Walsh, W. S., Thole, K. A., and Joe, C., 2006, "Effects of Sand Ingestion on the Blockage of Film-Cooling Holes," ASME Conference Proceedings, 2006(4238X), pp. 81-90.

[14] Crosby, J. M., Lewis, S., Bons, J. P., Ai, W., and Fletcher, T. H., 2008, "Effects of Temperature and Particle Size on Deposition in Land Based Turbines," Journal of Engineering for Gas Turbines and Power, 130(5), p. 051503.

[15] Delimont JM, Murdock MK., Ng WF, Ekkad, SV, 2014, "Effect of Temperature on Microparticle Rebound Characteristics at a Constant Impact Velocity," Submitted to ASME Turbo Expo 2014, ASME, Dusseldorf, Germany.

[16] Nealy, D., Mihelc, M., Hylton, L., Gladden, H., 1984, "Measurements of Heat Transfer Distribution Over the Surfaces of Highly Loaded Turbine Nozzle Guide Vanes," Journal of Engineering for Gas Turbines and Power, 106, pp. 149-158.

[17] Hylton, L., Nirmalan, V., Sultanian, B., Kaufman, R., 1988, "The Effects of Leading Edge and Downstream Film Cooling on Turbine Vane Heat Transfer," NASA Contractor Report 182133.

[18] Hinkley, D. V., 1969, "On the Ratio of Two Correlated Normal Random Variables," Biometrika, 56(3), pp. 635-639.

[19] Delimont JM, Murdock MK., Ng WF, Ekkad, SV, 2014, "Effect of Near Melting Temperature on Microparticle Rebound Characteristics at a Constant Impact Velocity," Submitted to ASME Turbo Expo 2014, ASME, Dusseldorf, Germany.

[20] Whitaker S.M., Reilly D., Bons J.P, and Crafton, J., "A Survey of Airborne Particle Impact Characteristics Using High Speed Particle Shadow Velocimetry," AIAA 2013-2484

[21] Morrison F.A., "Data Correlation for Drag Coefficient for Sphere," Department of Chemical Engineering, Michigan Technological University, Houghton, MI 49931, www.chem.mtu.edu/~fmorriso/DataCorrelationForSphereDrag2010.pdf

8 Attribution

This project was completed as a team under the guidance of Rolls Royce. The experimental portion of the project was advised by Dr. Wing Ng and Dr. Srinath Ekkad. The setup, testing, and analysis detailed in this thesis was performed by Jacob Delimont and I. Jacob was the experimental team leader and deserves credit for his contributions. Without Jacob's knowledge this study would not have been completed. Avi Friendman, Raul Otero, and David Mayo assisted in the setup, testing, and data reduction portions of the study.

I was on this project for over a year and made significant contributions to the study and experimental setup. Some of the various projects that I oversaw and completed include: design and fabrication of a safety cage, design and fabrication of a support structure for a valve, assisting in the design of new equilibration pipes, updating CAD models, design and installation of an exhaust quenching system, design and installation of an upstream mass flow rate measuring system, assisting in the design and installation of a camera cooling system, assisting in the design and installation of the mass flow control valveing assembly, writing and rewriting data reduction code in Matlab, writing a particle counter code in Matlab, installation and debugging of different instrumentation, and overseeing installation of a second particle hopper. In addition to these projects I also helped and oversaw running the experiments and performing general maintenance on the VT Aerothermal Rig.

A. Appendix: Polynomial Curve Fit Data

Table 12. Polynomial Coefficients for 28 m/s Data

28 m/s	Total					
Temp. (K)	**a5**	**a4**	**a3**	**a2**	**a1**	**a0**
Amb.	1.157E-10	-7.876E-08	1.357E-05	-8.913E-04	1.615E-02	7.836E-01
873	-6.343E-10	2.159E-07	-2.568E-05	1.419E-03	-4.291E-02	1.261E+00
1073	1.201E-09	-3.521E-07	3.876E-05	-1.894E-03	3.301E-02	7.219E-01
28 m/s	**Normal**					
Temp. (K)	**a5**	**a4**	**a3**	**a2**	**a1**	**a0**
Amb.	1.480E-09	-4.048E-07	4.039E-05	-1.683E-03	1.784E-02	8.200E-01
873	-3.858E-09	1.040E-06	-1.076E-04	5.491E-03	-1.503E-01	2.474E+00
1073	1.306E-09	-3.719E-07	3.703E-05	-1.382E-03	2.289E-03	1.164E+00
28 m/s	**Tangential**					
Temp. (K)	**a5**	**a4**	**a3**	**a2**	**a1**	**a0**
Amb.	6.472E-10	-1.268E-07	1.082E-05	-4.794E-04	6.269E-03	8.255E-01
873	8.068E-09	-1.767E-06	1.418E-04	-5.062E-03	7.307E-02	4.232E-01
1073	7.189E-09	-1.640E-06	1.420E-04	-5.720E-03	1.012E-01	2.030E-01

Table 13. Polynomial Coefficients for 70 m/s Data

70 m/s	Total					
Temp. (K)	**a5**	**a4**	**a3**	**a2**	**a1**	**a0**
1073	1.463E-09	-4.081E-07	4.411E-05	-2.188E-03	4.043E-02	5.848E-01
1173	4.540E-09	-1.074E-06	9.719E-05	-4.141E-03	7.501E-02	3.195E-01
1223	-2.760E-10	1.686E-07	-2.548E-05	1.601E-03	-5.119E-02	1.394E+00
1273	3.925E-09	-1.035E-06	1.064E-04	-5.231E-03	1.143E-01	-1.072E-01
1323	3.111E-10	-7.436E-08	6.681E-06	-2.556E-04	-2.933E-03	9.034E-01
70 m/s	**Normal**					
Temp. (K)	**a5**	**a4**	**a3**	**a2**	**a1**	**a0**
1073	-2.787E-09	7.045E-07	-7.054E-05	3.608E-03	-1.013E-01	1.802E+00
1173	6.074E-09	-1.502E-06	1.417E-04	-6.263E-03	1.219E-01	-1.700E-01
1223	-5.605E-09	1.588E-06	-1.735E-04	9.193E-03	-2.444E-01	3.283E+00
1273	9.804E-09	-2.595E-06	2.625E-04	-1.243E-02	2.618E-01	-1.209E+00
1323	-1.112E-08	3.050E-06	-3.253E-04	1.687E-02	-4.305E-01	4.899E+00
70 m/s	**Tangential**					
Temp. (K)	**a5**	**a4**	**a3**	**a2**	**a1**	**a0**
1073	4.414E-08	-1.065E-05	9.879E-04	-4.380E-02	9.166E-01	-6.443E+00
1173	3.876E-08	-9.173E-06	8.303E-04	-3.569E-02	7.193E-01	-4.659E+00
1223	6.344E-09	-1.274E-06	9.102E-05	-2.644E-03	1.929E-02	8.578E-01
1273	6.48E-09	-1.24E-06	8.24E-05	-0.0021074	0.0080319	0.9305862
1323	2.33E-08	-5.68E-06	0.000532	-0.02386	0.50787	-3.38771

B. Appendix: Rig Improvements

Burner Insert

A problem was encountered with the VT Aerothermal Rig when testing with low mass flow rate conditions at 800°C. At the low mass flow rate needed to achieve a flow velocity of 28 m/s, the burner could not produce a temperature of 800°C at the test coupon. It was concluded that the combustion process occurring at stoichiometric fuel/air proportions. The problem was found to be an extremely large percent of the fuel energy was lost to the water jacket at very low mass flow rates. It was calculated that only 30% of the energy was going to the air and the other 70% was lost to the water jacket using equations 11 and 12. Table 14 shows the values used to determine the heat transfer to the air and water.

11) $$\dot{Q}_{air} = \dot{m}_{air} * \Delta h_{air}$$

12) $$\dot{Q}_{water} = \dot{m}_{water} * c_p * \Delta T_{water}$$

Table 14. Values used to determine the heat transfer to the air and water

Property	Air Value	Water Value
$\dot{m}$ (kg/s)	0.04	11.39
h_1 (kJ/kg)	300.19	--
h_2 (kJ/kg)	910.56	--
c_p (kJ/kg*K)	--	4.18
T_1 (°C)	20	20
T_2 (°C)	800	21.333

To solve this issue, a stainless steel pipe of 10" diameter was inserted into the back end of the burner, which is 12" in diameter. Figure 31 shows a diagram of the inside of the burner. The pipe was inserted to create an air gap between the main air flow and the

water jacket. Inserting the pipe increased the maximum temperature at the low mass flow rate from 650°C to ~850°C. Figure 32 shows a picture of the pipe insert in the burner.

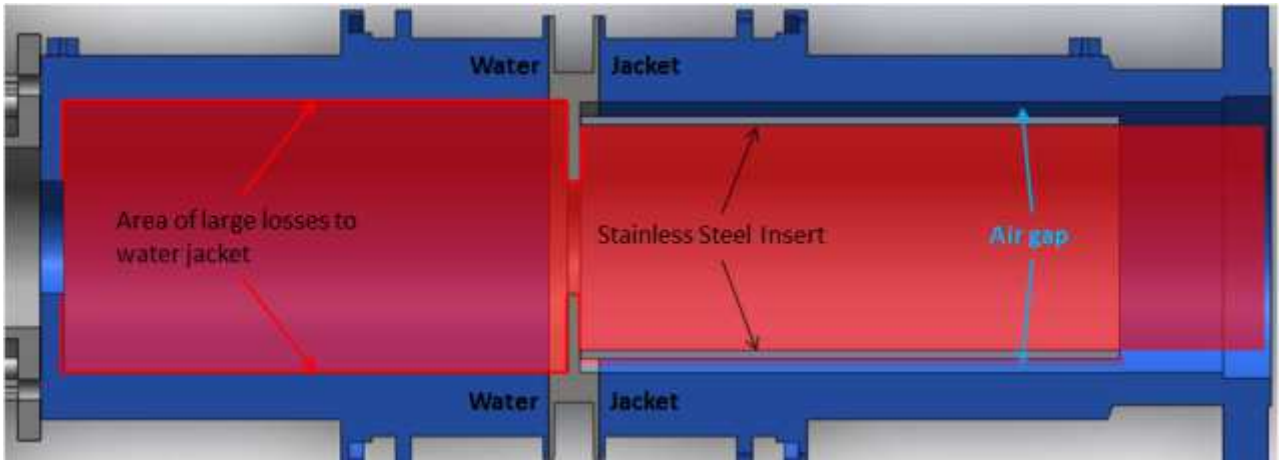

Figure 31. Cutaway of the water-cooled burner with the stainless steel insert

Figure 32. Picture of the stainless steel pipe insert in the burner.

Cooling Tower Insulation

The cooling tower is an expensive piece of equipment that is used to cool the cooling water used for the water-cooled burner. 2" PVC pipes carry the water from the burner to the cooling tower outside. During testing in the winter months the cooling tower is drained between testing to ensure that the water will not freeze and damage the components of the cooling tower. There wre concerns that all of the water was not draining from the PVC pipes and that ice was accumulating in the pipes while not testing. Insulation was added to the external portion of the PVC pipes to prevent freezing of the water. Figure 33 shows a picture of the insulation on the PVC pipes that connect to the cooling tower.

Figure 33. Picture of the added insulation on the cooling tower pipes

Safety Cage

The VT Aerothermal Rig is capable of running at extremely high temperatures of +1000°C. At these extreme temperatures safety precautions are a primary concern. Previously the only object preventing someone from coming in contact with a hot flange was a safety rope with 'danger hot' signs attached to the ropes. This safety precaution was deemed unacceptable and a safety cage was decided on to be the best option to prevent accidents. The safety cage had several requirements it needed to meet. It had to cover the entire length of the equilibration pipe, be light enough for two people to maneuver, and to adequately cover the piping while still being able to monitor the piping.

Designs for the safety cage were made in Solidworks. Figure 34 shows an isometric view of the safety cage. Figure 35 shows three standard views and dimensions of the safety cage for fabrication. The cage was constructed from 2" x 2" x 1/8" steel 90° angle iron, 2" x 1/8" steel rectangular bar, and steel expanded mesh. Figure 36 shows the finished safety cage covering the equilibration tube. Safety signs were added to the cage to add more safety.

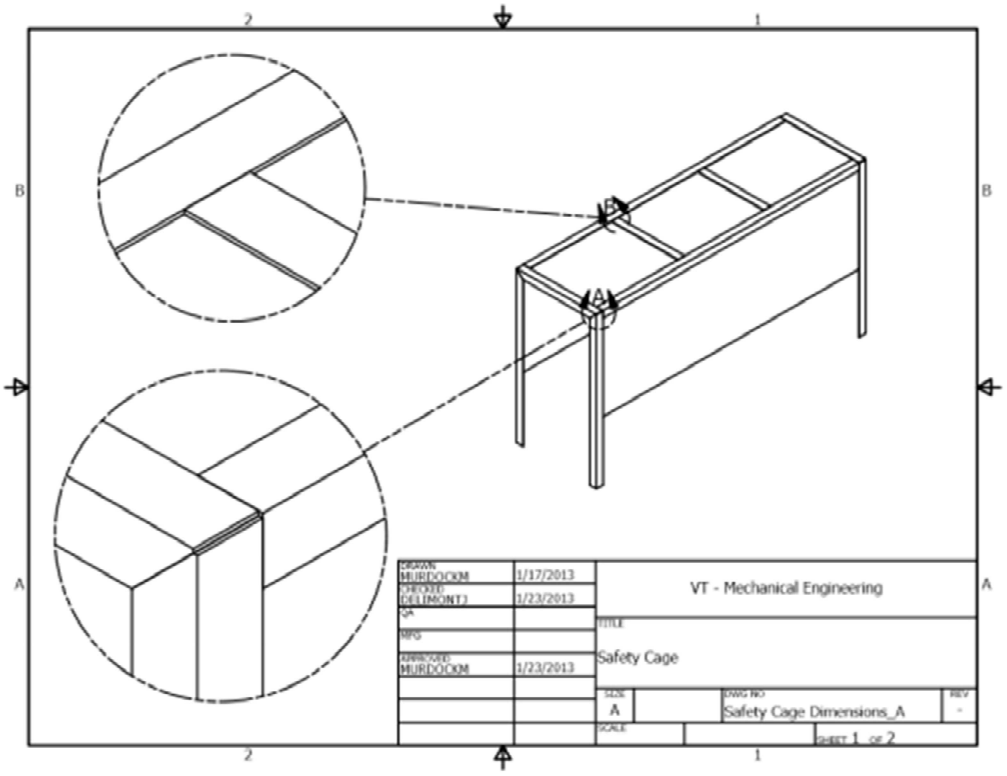

Figure 34. **Isometric view of the safety cage**

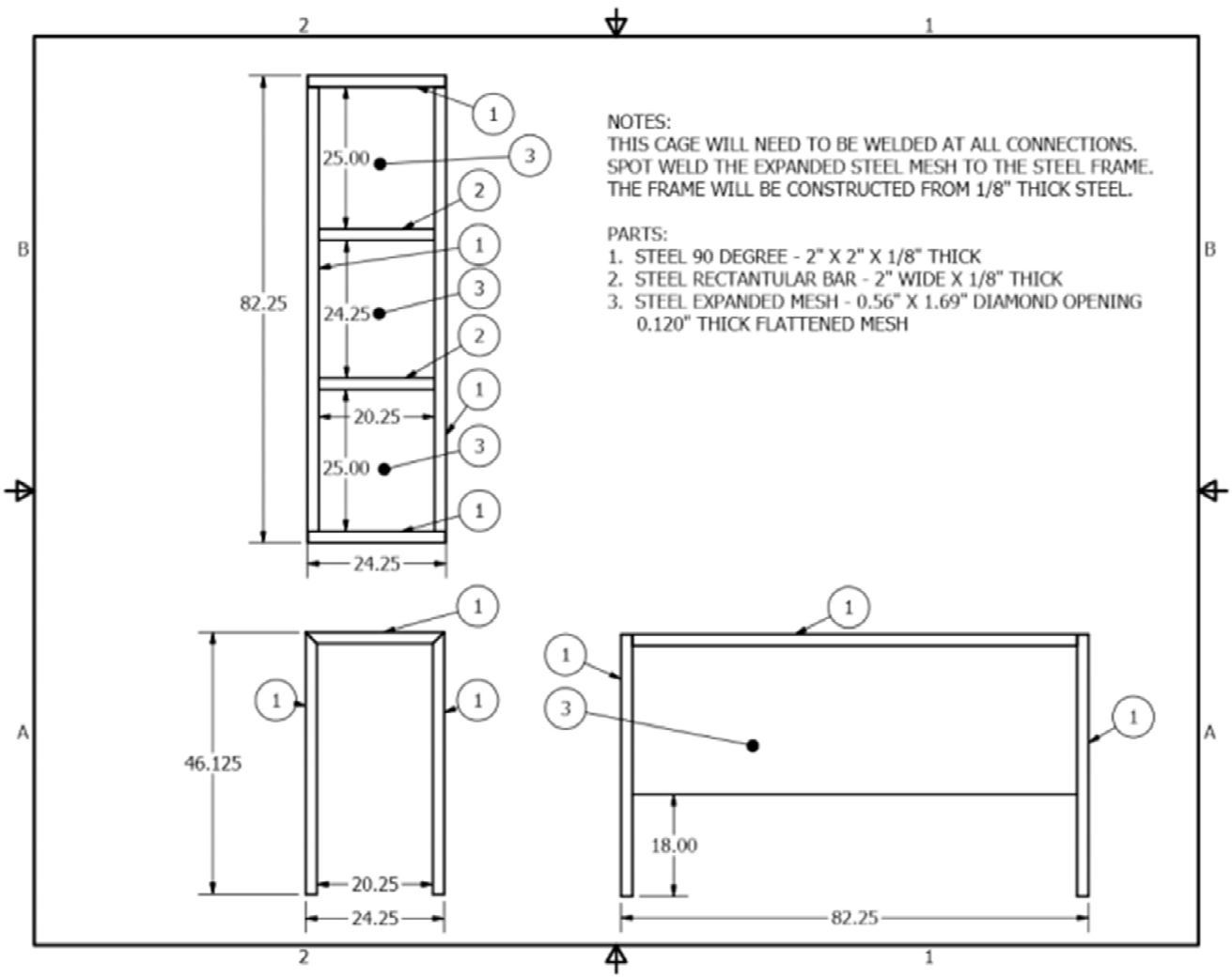

Figure 35. Views and dimensions of the safety cage

Figure 36. Picture of the safety cage